Department of Physics and Astronomy
University of Heidelberg

Bachelor Thesis in Physics
submitted by

Sebastian Spaniol

born in Trier (Germany)

February 2018

Electron Transport System for Fast-Timing-Readout at a Micro-Calorimeter Particle Detector

This Bachelor Thesis has been carried out by Sebastian Spaniol at the
Max Planck Institute for Nuclear Physics in Heidelberg
under the supervision of
Dr. Oldřich Novotný and Apl. Prof. Dr. Andreas Wolf

Abstract

The micro-calorimeter particle detector MOCCA is dedicated for position- and mass-resolved detection of neutral molecular fragments produced in electron–ion interactions at the Cryogenic Storage Ring at the Max Planck Institute for Nuclear Physics in Heidelberg. A feasibility study is performed for 3D fragment-imaging to determine the kinetic energy released in the fragmentation. For this purpose, impact time measurement on a ns scale will be necessary in addition to the position measurement and is planned to be realized by fast-timing-readout of secondary electrons. Simulations of the employed electrostatic electron transport system are presented in this thesis, qualitatively approving the proposed concept. Within simulations at a realistic model of the electron transport system, a narrow electron time-of-flight distribution was found with a width of $\approx 30\,\mathrm{ps}$, proving the expectation of conserved timing information of fragments by secondary electrons. Assignment of timing information to its corresponding fragments was found to be likely possible under restriction of minimum distance between impinged fragments in the range of 3.64 mm to 5.06 mm, compared to the detection area of $44.8\,\mathrm{mm} \times 44.8\,\mathrm{mm}$.

Zusammenfassung

Der mikro-kalorimetrische Teilchendetektor MOCCA ist dem positionsauflösenden Detektieren von neutralen Molekülfragmenten gewidmet, die durch Interaktionen zwischen Elektronen und Molekülionen am Kryogenen Speicherring am Max-Planck-Institut für Kernphysik in Heidelberg produziert werden. Um die gesamte kinetische Energie zu bestimmen, die bei der Molekülfragmentation freigesetzt wird, wird eine Studie zum 3d Imaging der Fragmente an dieser Anlage durchgeführt. Hierfür ist zusätzlich zur Positionsmessung eine Messung der Auftreffzeiten im ns-Bereich nötig, welche durch ein fast-timing-readout von Sekundärelektronen ermöglicht werden wird. Dazu wurde ein elektrostatisches Elektronentransportsystem erdacht und in Simulationen getestet, welche in der vorliegenden Arbeit präsentiert werden und das erdachte Konzept qualitativ bestätigen. In Simulationen an einem realistischen Modell des Elektronentransportsystems wurde eine schmale Verteilung von Elektronen-Flugzeiten festgestellt, dessen Breite von $\approx 30\,\mathrm{ps}$ zu der Erwartung führt, dass die Timing-Informationen der Molekülfragmente durch die Sekundärelektronen erhalten werden. Eine Zuordnung der Timing-Informationen zu ihren zugehörigen Fragmenten wurde als wahrscheinlich möglich eingestuft, sofern die aufgetroffenen Fragmente einen minimalen Abstand im Bereich von 3.64 mm bis 5.06 mm im Vergleich zur Detektionsfläche von $44.8\,\mathrm{mm} \times 44.8\,\mathrm{mm}$ aufweisen.

Acknowledgement

I would like to thank:

Dr. Oldřich Novotný for his supervision with a mentoring attitude throughout the whole project of simulations of the electron transport system for MOCCA,

Apl. Prof. Dr. Andreas Wolf for his guided tour at CSR, at which my interest for this project arose, and furthermore for his kind supervision of the working group with me as member,

Prof. Dr. Klaus Blaum for the welcoming initiation into his scientific division,

my division colleagues for the friendly atmosphere,

the MPIK for the utilization of its infrastructure,

and my friends Anna, Florian and Marc for their constructive feedback on this thesis.

Moreover, for the time throughout the course of studies I would like to thank :

my family for supporting me,

all my friends for taking care of me in their individual ways,

and especially my friend Nicole and my brother Philipp for their profound support.

Contents

List of Abbreviations

CMF	center of mass frame
CSR	Cryogenic Storage Ring
ETS	Electron Transport System
FWHM	full width at half maximum
HWHM	half width at half maximum
KER	kinetic energy released
MCP	micro-channel plate
MOCCA	MOleCular CAmera
MPIK	Max Planck Institute for Nuclear Physics
p.d.f.	probability distribution function
TOF	time-of-flight

1 Introduction

In the first session of his today well known Lectures on Physics, Richard Feynman stated the following: "If, in some cataclysm, all of scientific knowledge were to be destroyed, and only one sentence passed on to the next generations of creatures, what statement would contain the most information in the fewest words? I believe it is the atomic hypothesis (or the atomic fact, or whatever you wish to call it) that all things are made of atoms—little particles that move around in perpetual motion, attracting each other when they are a little distance apart, but repelling upon being squeezed into one another."[1]

In 1963, when Feynman began holding his lectures, the atomic hypothesis had been acknowledged to be true for several decades already. Nevertheless, the atom itself still constitutes as a profound subject in today's research. The CSR experiment (Cryogenic Storage Ring [2]) is dedicated for exploration of molecular reactions under interstellar conditions, similar to those prevailing in interstellar clouds. The aim is to provide insight to the submicroscopic many-body quantum dynamics inside the molecules under such conditions. The CSR is located at the MPIK (Max Planck Institute for Nuclear Physics in Heidelberg, Germany), at which this thesis has been carried out. The goal of this thesis is to provide simulations for improvement of one of the particle detectors at CSR, which is described in the following.

1.1 Fragmentation Experiments

Quantum dynamics, as a wide subject of scientific research, may be investigated by a broad variety of means. In fragmentation experiments, molecules undergo certain reactions and are thereby divided into molecular and sub-molecular pieces as governed by their internal quantum dynamics. This quantum dynamics can be studied by measurements on the resulting products. One type of molecular reactions is dissociative recombination. The energy scheme of a dissociative recombination with the corresponding reaction equation

$$\mathrm{AB}^+ + \ e^- \ \rightarrow \ \mathrm{A} + \mathrm{B} \tag{1}$$

is exemplary shown for a two-body-fragmentation[1] in fig. 1. When brought into contact with electrons, molecular cations AB^+ are given the chance to recombine. A collision between electron and cation provides the energy E_{col}, leading towards the excited state AB^*. Afterwards a dissociation process gives rise to the electrically neutral fragments A and B, with the total kinetic energy released E_{KER} in this process. These products may also occupy excited states with the final state energy

$$E_{\mathrm{p}} = E_{\mathrm{col}} - E_{\mathrm{KER}} \quad . \tag{2}$$

This final state energy is a desired key information for studying quantum dynamics of molecular reactions. At the CSR, dissociative recombination is realized in the electron-ion

[1] The presented concepts may be extended from two-body-fragmentation to many-body-fragmentation.

interaction zone of the experiment, as indicated in fig. 2. After injection at 300 keV from an ion-chemistry high-voltage platform, the molecular ions are kept on a closed orbit by an electrostatic ion-optical system, consisting of deflectors and focusing elements. At the electron cooler a bath of electrons is provided, which are moving into the same direction as the molecular ions. The difference in velocities of electrons and molecular ions along the ion beam axis allows a precise control of the collision energy E_{col}. The desired final state energies E_{p} of molecular fragments may be obtained by measurement of the total kinetic energy released E_{KER}. For this purpose the fragments need to be detected, which is briefly described in the following.

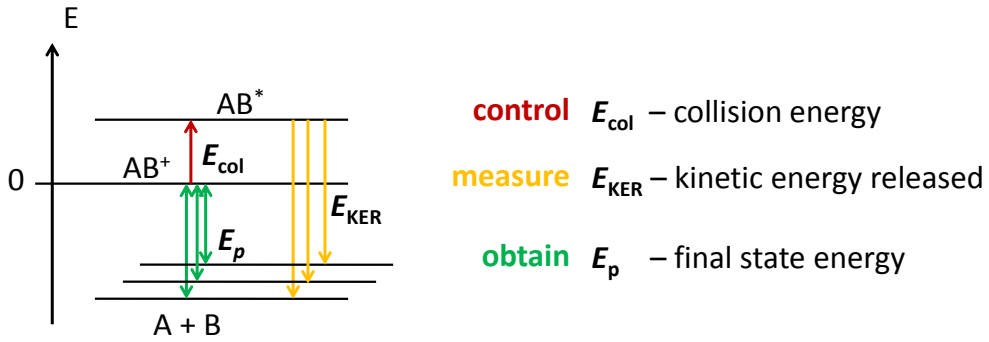

Figure 1: Energy scheme of a two-body-fragmentation through the capture of an electron of collision energy E_{col} on a molecular ion AB^+. From the intermediate state AB^* it fragments to yield products A + B. Varying energy releases E_{KER} reflect the final state energy E_{p}.

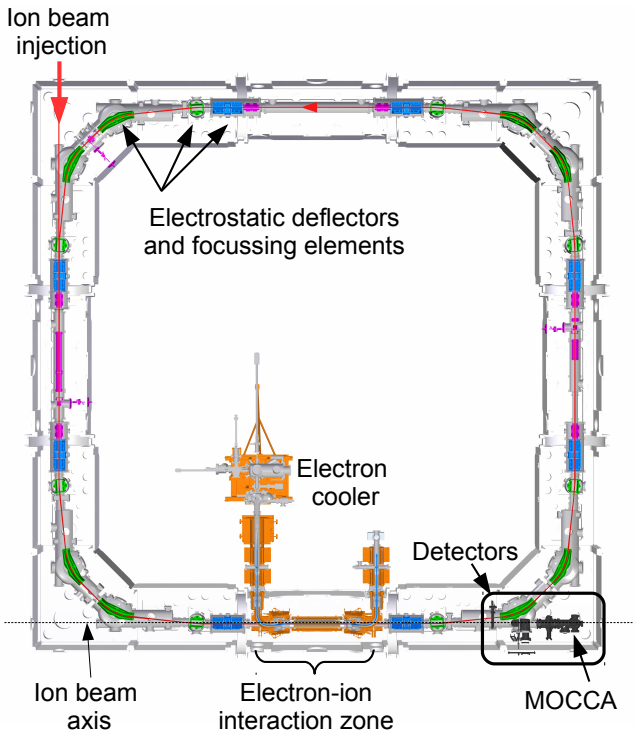

Figure 2: Schematic top-view onto the CSR. Molecular ions are injected at 300 keV and are kept on a closed orbit by an electrostatic ion-optical system. In the electron-ion interaction zone, a collision between electrons and molecular ions with controlled collision energy E_{col} gives rise to fragmentation processes. Several detectors are set up for fragment detection. The detector MOCCA will be described further in section 1.3.

1.2 Fragment Detection

The detection of fragments is illustrated exemplary for a two-body-fragmentation[2] in fig. 3. As conservation of momentum is fulfilled, fragments of different masses have velocity vectors of opposite direction but of different length depending on the masses. In the lab frame, the center of mass is still moving with the ion-beam velocity $\mathbf{v_{ion}}$. This is the same velocity the molecular ion had before the reaction with the electron. The velocity of fragments in the lab frame is therefore given by the superposition principle.

Placing a detector with planar detection area aligned at the ion beam axis (cf. fig. 2), the two fragments will impinge on this detector. The transversal velocity components will give rise to a spatial difference Δx on the detector, while the longitudinal velocity components will give rise to a difference Δt in the arrival times at the detector. With

[2]The detection principle remains the same for cases of many-body-fragmentations.

a position measurement and a timing measurement, all velocity components of the fragments can be reproduced. Together with an examination of the fragment masses, this 3D fragment-imaging would enable a determination of the total kinetic energy released at the dissociative recombination. Moreover, if not only the timing difference but also the mass-sorted order of the fragment arrival at the detector can be determined, the orientation of the fragmentation process in three-dimensional space could be deduced. This would give further insight in the quantum dynamics of such fragmentation processes.

From the atomic masses of molecules and the typical kinetic energy released in the regime of 1 eV, the typical difference of arrival times of fragments is deduced to be in the regime of $\Delta t \lesssim 100\,\mathrm{ns}$. Depending on the orientation of the fragmentation, this difference may lower towards zero. Thus a fast-timing-readout system is necessary for the timing measurement.

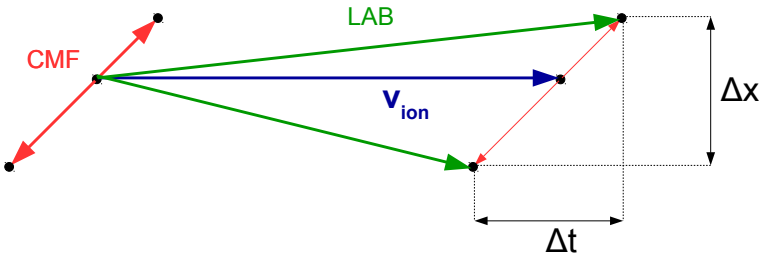

Figure 3: Exemplary illustration of a two-body-fragmentation. In this example the two fragments have different masses. Their velocities in the center of mass frame (labeled as CMF) are represented by the red arrows. In the laboratory frame (LAB), the center of mass is moving with the original ion beam velocity $\mathbf{v_{ion}}$, represented by the blue arrow. Note that this illustration is not in scale, since for the amplitudes of velocities $v_{\mathrm{ion}} >> v_{\mathrm{CMF}}$ is true. The resulting velocities of fragments in the lab frame are represented by the green arrows. When the fragments impinge on a detector, their transversal velocity components give rise to a spatial difference Δx, while their longitudinal velocity components give rise to a timing difference Δt.

1.3 MOCCA

For detection of molecular fragments at the CSR, the detector MOCCA (MOleCular CAmera) is under development. The dedicated location of MOCCA at the CSR is indicated in fig. 2. The concept of this detector and preparing investigation of its underlying physical principles have been discussed in detail by Novotný, Gamer et al.[3, 4]. MOCCA is a micro-calorimeter particle detector. When a fragment impinges on it, the laboric kinetic energy of the fragment is transferred to thermal energy. This gives rise to

a thermal pulse as schematically shown in fig. 4. The event of a thermal pulse initializes a measurement of the location of this pulse at the planar detection area. Thus a position measurement of fragments is enabled at MOCCA. For 3D fragment-imaging, MOCCA would ideally be capable of a timing measurement as well. As described above, the expected typical timing between fragments at MOCCA is in the regime of $\lesssim 100\,\mathrm{ns}$. Compared to that, the signal rise and signal decay time of a thermal pulse are larger in 1-4 orders of magnitude[4], as indicated in fig. 4. Therefore the relative timing between different fragments cannot be resolved by their corresponding thermal pulses. Thus MOCCA itself exhibits no resolution of timing information and a different strategy is necessary for timing measurement at the detector:

The detection surface of MOCCA is planned to be made of gold. Fragments impinging on it will induce secondary electrons. Detection of these electrons with an electron transport system and a fast-timing-readout system would reproduce the desired timing information. The concept of accelerating and guiding ion-induced secondary electrons towards a timing-detector has already been presented by De Cesare et al.[5]. A similar concept is considered for an electron transport system in order to enable 3D fragment-imaging at MOCCA. This is presented in the following.

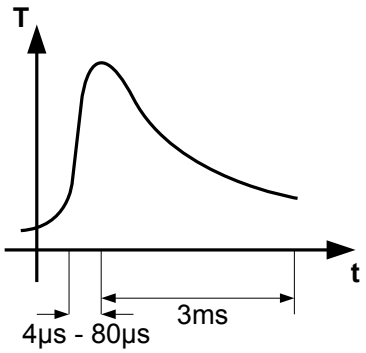

Figure 4: Scheme of a thermal pulse produced at MOCCA while impingement of a fragment. Abscissa shows the time t, ordinate shows the temperature T. The signal rise is in the regime of 4 µs to 80 µs, the signal decay time is in the regime of 3 ms [4]. Compared to the expected typical difference of $\lesssim 100\,\mathrm{ns}$ in arrival times of fragments at MOCCA, thermal pulses of different fragments are not capable of resolving the timing information of these fragments. Thus a different strategy is necessary for timing measurement at MOCCA.

1.4 Goal of this Thesis

An electrostatic device for guiding secondary electrons from the detection area of MOCCA towards a timing detector is thought of in form of an electron transport system (ETS). A basic scheme of this ETS is shown in fig. 5. Following this concept, electrons induced by fragments at MOCCA are accelerated by an acceleration harp. MOCCA is set at ground potential, while a potential of 5 kV is applied onto the acceleration harp. The same potential of 5 kV is applied onto the drifttube, such that its inner region would ideally be free of any electric field disturbing the electrons. The internal mirror harp is set to 5 kV as well, while the external mirror harp is set at ground potential. Thus the external mirror harp is repulsive for electrons and due to the orientation of the mirror, the electrons are bent at an angle of 90°.

Originally grids instead of harps were used for acceleration and bending of electrons by De Cesare et al.[5] For the ETS presented in fig. 5, the wires normal to the plane of the shown scheme were removed. Because of the finite dimensions of these wires, their angle of 45° towards the beam axis would lower the transmittance of the electron mirror for incoming fragments. If the wires were infinite small, this would be no problem.

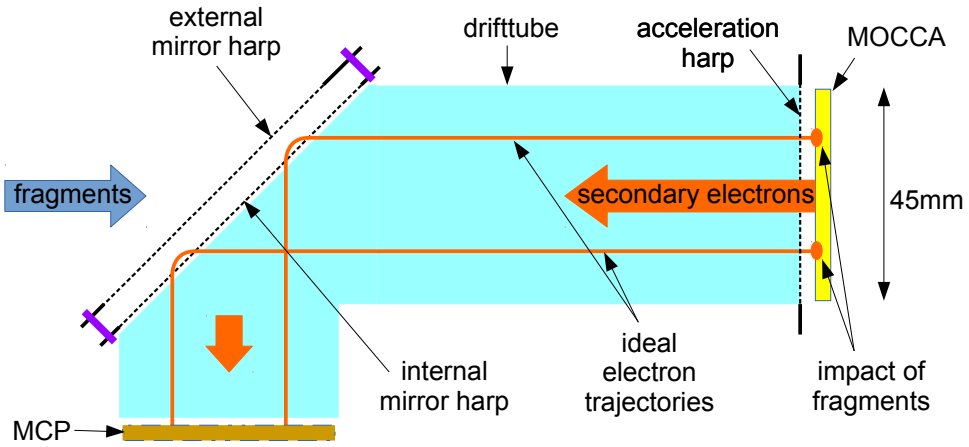

Figure 5: Scheme of the electron transport system (ETS). Secondary electrons are induced at the gold surface of MOCCA when molecular fragments impinge. These electrons are accelerated and guided towards an MCP (micro-channel plate). Because the MCP would otherwise block incoming fragments, electrons need to be bent at an angle of 90° with an electron mirror. The electron trajectory length is conserved for various origin positions and therefore the incoming electrons at the MCP are supposed to reproduce the relative impact times of the fragments.

After the electrostatic mirror, the electrons continue towards the MCP (micro-channel plate), constituting as timing detector and also set to 5 kV. Impingement of an electron at the MCP will give rise to an electron cascade. This will produce a measurable voltage pulse at the MCP. Voltage pulses from different electrons are capable of resolution of the difference in arrival times of electrons at the MCP. In contrast to the thermal pulses at MOCCA, these voltage pulses at MCP are therefore able to reproduce the timing information of fragments.

A precondition for this reproduction of timing information is the conservation of timing information by secondary electrons. For this purpose the variance in TOF (time-of-flight) of electrons traversing the ETS would need to be small compared to the typical timing of fragments, which is in the regime of $\Delta t \lesssim 100\,\mathrm{ns}$. The concept of the ETS in fig. 5 would theoretically ensure the same trajectory length for all electrons starting at normal incident from MOCCA, giving rise to almost the same TOF for all those electrons. The electron cascade at the MCP will also produce a light spot at a phosphor screen set behind the MCP. The phosphor screen thus enables position measurement of secondary electrons.

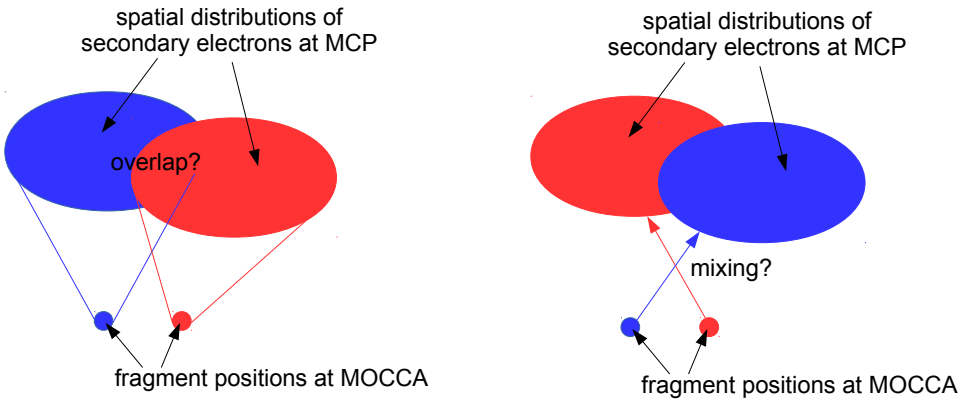

Figure 6: Schemes of complications for the mapping process between MCP and MOCCA. A secondary electron induced by a fragment has different possible initial velocity vectors. This would give rise to a possible spatial electron distribution at the MCP, i.e. distribution of possible final positions. Electrons at the MCP would need to be correctly assigned to their induced fragments at MOCCA in order to make use of the timing information. This assignment would be complicated if spatial electron distributions from different fragments would a) overlap or b) be mixed. This would also be complicated if more than one electron per fragment were induced.

This is a necessary feature, because the voltage pulses at the MCP contain the information of relative timing difference between two fragments, but they do not contain the information to which two fragments this relative timing difference corresponds.[3] Thus a mapping process between MOCCA and MCP is necessary, in which each secondary electron at MCP is correctly assigned to its inducing fragment at MOCCA. If the electron positions at MCP were projected at MOCCA, the electrons and their corresponding fragments would ideally share the same position. This is assumed to be true for the trajectories indicated in fig. 5, therefore these trajectories are called "ideal". But this assignment is not trivial due to the possible initial velocity vectors of secondary electrons: Possible secondary electrons from the same fragment at MOCCA would distribute at different positions at MCP. This is illustrated in fig. 6. An overlap or mixing of two spatial electron distributions at MCP for two fragments at MOCCA would make the mapping process difficult. The greater the overlap, the less likely the mapping would be successful for individual events in the case of no mixing.

The goal of this thesis is to perform a feasibility study of the ETS by means of simulations. The two concerns are namely: Firstly, is the timing information of fragments conserved by the secondary electrons in the ETS? Secondly, is a mapping process between MOCCA and MCP possible in order to assign the timing information to its corresponding fragments? For the purpose of addressing these two major questions, simulations of electron trajectories in a modeled ETS are necessary. The required data are TOF, initial position and final position of simulated electrons. For calculation of realistic trajectories of electrons induced by fragments, physical initial conditions of secondary electrons are to be implemented in these simulations. At first a simplified model of the ETS is simulated in order to examine the influence of individual components of the ETS on electron trajectories. Further simulations at a realistic model of the ETS are then needed for testing the feasibility of the ETS under realistic conditions.

[3] The two-body-fragmentation is the only exception to this. But even in this case the timing difference alone cannot tell at which order the fragments arrived at MOCCA.

2 Physical Principles

Before a first simulative approach is presented in section 3, the underlying theoretical foundations are introduced. This gives rise to the following essential questions: Beginning with the impingement of a neutral fragment into MOCCA, secondary electrons may be produced in this process. Especially their angle towards the detector's surface and their kinetic energy are important to consider for calculation of realistic electron trajectories in the ETS. Therefore section 2.1 deals with the question: "What are the production mechanisms and resulting initial conditions for secondary electrons at metal surfaces?"

Instantly after the production of secondary electrons, the ETS guides the electrons towards the MCP by electrostatic fields. This guiding was simulated by the software package SIMION (Scientific Instrument Services, Inc. (SIS) [6]). Therefore section 2.2 deals with the question: "What is the physics on which the ETS and simulations by SIMION are based on?"

2.1 Production Mechanisms and Initial Conditions of Secondary Electrons

It is a well-known phenomenon that secondary electrons are emitted from a solid, especially a metallic surface when it undergoes bombardment by energetic particles. Often this is described by "ion-induced secondary electron emission" [7], but in spite of the ionic reference it also includes bombardment by electrically neutral particles. Therefore secondary electrons will also be induced when molecular fragments impinge the gold surface of MOCCA. The case in which direct transfer of kinetic energy from the projectile into the target gives rise to electron emission is schematically shown in fig. 7a. This is called "kinetic electron emission" and consists of three steps [7]:

Firstly, excited electrons are generated in the solid, but not all excited electrons give rise to secondary electron emission. At ion beam energy of 300 keV, which is in the regime of high impact energies, the main production mechanisms are contributions from electrons of the target: excitation of conduction electrons from the Fermi-edge on the one hand, and ionization of inner-shell electrons on the other hand. Secondly, parts of the excited electrons diffuse towards the surface. On their way, they loose previously gained energy by colliding with other electrons in the target and may hereby multiply in a cascade. Thirdly, electrons penetrate through the surface into the vacuum. This is considered as a refraction process.

Compared to the dimensions of the detection area of MOCCA, the electrons do not propagate far away from the entrance point of the projectile. Thus it is approximated that secondary electrons emit at the the same point as the projectile has entered, as shown in fig. 7b. In the same figure, it is also indicated that secondary electrons will have different initial velocity vectors. The possible direction and amplitude of the velocity vectors are represented by the distribution of the polar angle ϑ to the surface normal (cf. fig. 7a) and the distribution of kinetic energy. Experiments at impact energies up to 5 keV found the following distribution of polar angle ϑ of emitted secondary electrons

from clean solid surfaces impinged by projectiles at normal incident[7]:

$$\frac{\mathrm{d}\gamma}{\mathrm{d}\Omega}(\vartheta) = \left.\frac{\mathrm{d}\gamma}{\mathrm{d}\Omega}\right|_{\vartheta=0} \cdot \cos(\vartheta) \tag{3}$$

Here γ denotes the total yield of electrons emitted into the half sphere in front of the target. For H^+ impact on a gold target, a mean total electron yield of 2.2 electrons per impinging particle was found [8]. The normal incident of impinging projectiles is approximately true for molecular fragments at MOCCA (cf. description of fig. 3 in section 1.2). In this thesis it is assumed that the angular distribution as stated in eq. (3) will not change significantly for higher impact energies, such as the 300 keV ion beam energy at CSR. In addition to that, no dependency on the azimuthal angle was experimentally found, which is expected due to the isotropic structure of the solid.

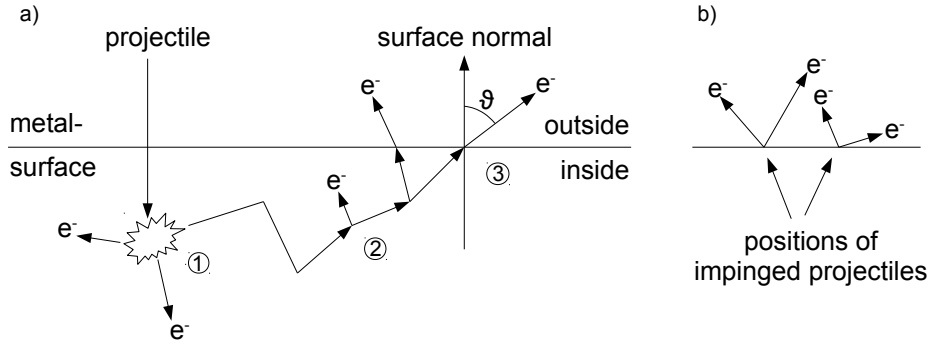

Figure 7: Schemes of kinetic electron emission.
a) The production mechanism of secondary electrons is illustrated on a microscopic scale and consists of three steps: (1) Excitation of electrons in the target, (2) diffusion of excited electrons towards the surface, (3) penetration of the electrons through the surface.
b) Secondary electrons have different initial velocity vectors. Considering the dimensions of the detection area of MOCCA, the position of an emitted electron is approximately equal to the entering position of its parent fragment on a macroscopic scale.

The spectra of kinetic energy E of ion-induced secondary electrons emitted from different types of clean metal surfaces under bombardment of different species of projectiles with different projectile energies were investigated by Hasselkamp et al.[9]. They found that the secondary electron distributions depend on the target material, on the projectile species, and on the projectile energy as well. However, the form of the distribution was found to be similar for all projectile-target combinations tested. Electron energies are found mostly in the low energy regime, i.e. below 200 eV with the greatest yield between 0 eV to 60 eV [9]. For a gold target under bombardment with H^+ at 300 keV impact

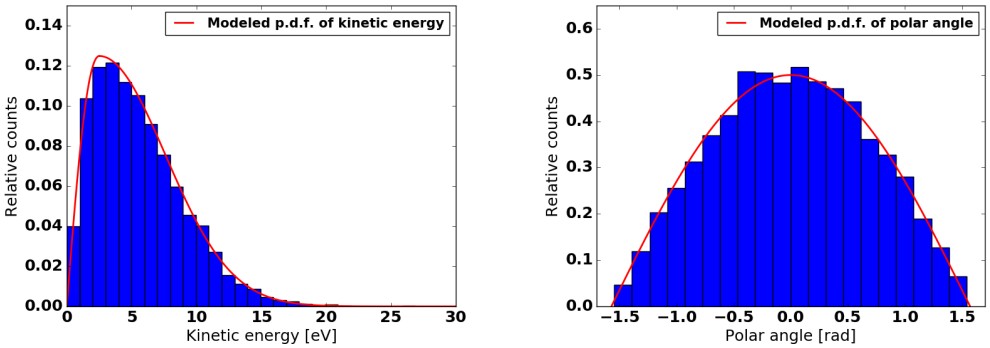

(a) (b)

Figure 8: Plots of distribution of a) initial kinetic energy E and b) initial polar angle ϑ for 10 000 simulated secondary electrons in SIMION. The red curves show the corresponding probability distribution functions (p.d.f.). The p.d.f. of E was modeled based on experimental data from [9] (c.f. eq. (6)). The p.d.f. of ϑ was given in [7] (c.f. eq. (3)). Normalized histograms of simulated electrons are in accordance with both p.d.f.s. Thus the implementation of physical initial conditions of secondary electrons in SIMION was successful.

energy, Hasselkamp et al. give two parameters of the resulting energy spectrum [9]: Firstly, the maximum of the spectrum is located at $E_{\max} = 2.5\,\mathrm{eV}$. Secondly, the full width of the spectrum as measured at half maximum is located at $\Delta_{1/2} = 8.5\,\mathrm{eV}$. The shape of the spectrum as shown in fig. 8a indicates that an evaluation of the half width at half maximum

$$\mathrm{HWHM} = \Delta_{1/2} - E_{\max} \tag{4}$$

is only possible for energies $E \geq E_{\max}$. Because an explicit energy distribution function was not given in [9], the probability distribution function (p.d.f.) of kinetic energy needed to be modeled. At first a Maxwell-Boltzmann distribution was considered for this purpose. But for this type of distribution no accordance to the value of $\Delta_{1/2}$ given in [9] could be achieved. Therefore a normal distribution was considered, because a normal distribution exhibits a definite dependency between the half width at half maximum HWHM and the standard deviation σ:

$$\mathrm{HWHM} = \sqrt{2\ln(2)}\;\sigma \tag{5}$$

Thus a normal distribution was implemented for energies $E \geq E_{\max}$, because only in this regime the HWHM can be defined as mentioned above. For energies $E < E_{\max}$ an modeling similar to a Rayleigh distribution was used, because this had greater qualitative accordance to the given spectrum in [9] than a Maxwell-Boltzmann distribution. Thus

the energetic p.d.f. was modeled as follows:

$$P(E) = \begin{cases} \frac{\nu}{\sqrt{2\pi\sigma^2}} \frac{E}{E_{\max}} \exp\left(\frac{1}{2}\left(1 - \frac{E^2}{E_{\max}^2}\right)\right) & E < E_{\max} \\ \frac{\nu}{\sqrt{2\pi\sigma^2}} \exp\left(-\frac{1}{2}\frac{(E-E_{\max})^2}{\sigma^2}\right) & E \geq E_{\max} \end{cases} \tag{6}$$

Here σ is given by eq. (4) and eq. (5), based on the experimental values of $E_{\max}$ and $\Delta_{1/2}$. The normalization factor $\nu = 1.594985$ was achieved numerically.

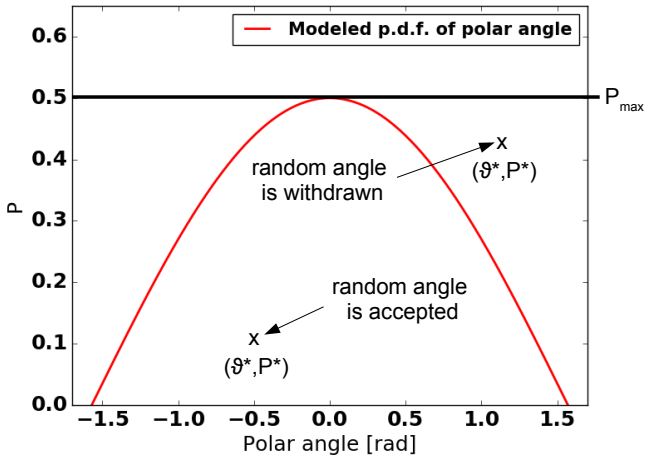

Figure 9: Illustration of the randomization method for implementation of initial conditions of secondary electrons in SIMION, specifically shown for the angular distribution. The interval of possible angle ϑ and the interval of its corresponding p.d.f. value P define a rectangle. In this rectangle, a random point $(\vartheta^*, \mathrm{P}^*)$ was generated using uniform probability distributions for ϑ^* and P^*. If this random point was in the area under the curve of the angular p.d.f., the corresponding random angle ϑ^* was accepted as initial angle for the currently simulated electron, otherwise this random point was withdrawn and a new random point was tested. The same method was used for implementation of the initial kinetic energy.

The implementation of initial conditions of electrons in the simulation program SIMION assumes that the initial electron energy and angle are independent and follow the distributions given by eq. (3) and eq. (6), respectively. The azimuthal angle is uniformly distributed. The Monte-Carlo approach is employed to generate the initial electron velocity vectors following these distributions, as demonstrated in fig. 8. For generating the randomized events following these non-trivial p.d.f.s a randomization method is used as illustrated in fig. 9:

As a first step, physical useful intervals for the angle ϑ and the energy E were chosen, namely $\vartheta \in [-\pi/2, \pi/2]$ and $E \in [0\,\mathrm{eV}, 300\,\mathrm{eV}]$. The maximum energy of electrons was chosen as 0.1 % of the ion beam energy of 300 keV, such that also cases of less likely electrons with energy $E > 200\,\mathrm{eV}$ were included in the simulations.

The actual method is based on the "Rejection method" for random number generation [10] and is described in the following specifically for the angular distribution by reference to fig. 9. The p.d.f. as given in eq. (3) was normalized such that integration over all possible polar angles yielded a total probability of 1. Denoting the p.d.f. value with P, possible values are between 0 and a maximum value $\mathrm{P}_{\max}$. For each electron a random point (ϑ^*, P^*) was produced using a uniform random number generator, with $\vartheta^* \in [-\pi/2, \pi/2]$ and $\mathrm{P}^* \in [0, \mathrm{P}_{\max}]$. If the random point (ϑ^*, P^*) was in the area described by the angular p.d.f., the random angle ϑ^* was implemented as initial angle for the currently simulated electron, otherwise ϑ^* was withdrawn and a new random point was produced. The same procedure was executed for the initial kinetic energy of each secondary electron.

2.2 Electrostatic Guiding of Secondary Electrons

The electrostatic guiding of secondary electrons in the ETS was simulated by the software package SIMION. A first ion-optical impression of a realistic model of the ETS is shown in fig. 10, where electrons started at normal incident are guided by the modeled ETS. Simulations of this realistic model will be discussed in further detail in section 4. The typical electron trajectories will most likely differ from the shown trajectories due to the initial conditions of secondary electrons (cf. section 2.1).

SIMION is capable of calculating the electron trajectories by considering the relativistic form of Newton's second law of motion [11]

$$\mathbf{F} = \frac{\mathrm{d}\mathbf{p}}{\mathrm{d}t} \quad , \tag{7}$$

where $\mathbf{F}$ is the net force acting upon one electron, $\mathbf{p}$ is the relativistic momentum of this electron, and t denotes time. In the case of the ETS, the net force $\mathbf{F}$ acting upon the electron is purely electrostatic when neglecting gravity. A short estimate will verify this: Newton's law of gravitation states that the magnitude of the force due to gravity between an electron and the earth will be

$$F_\mathrm{g} = G\frac{mM}{R^2} \quad , \tag{8}$$

where G is the gravitational constant, m the electron mass, M the mass of earth and R the radius of earth. Coulomb's law states that the magnitude of force exerted by an electric charge Q on an electron will be

$$F_\mathrm{e} = \frac{1}{4\pi\epsilon_0}\frac{eQ}{r^2} \quad , \tag{9}$$

where ϵ_0 is the electric constant and r is the distance between the charge Q and the electron. Due to the dimensions of the ETS, typical distances between the electrodes and the electron will be in the regime of $r = 1\,\mathrm{cm}$. The electrodes of the ETS carry at

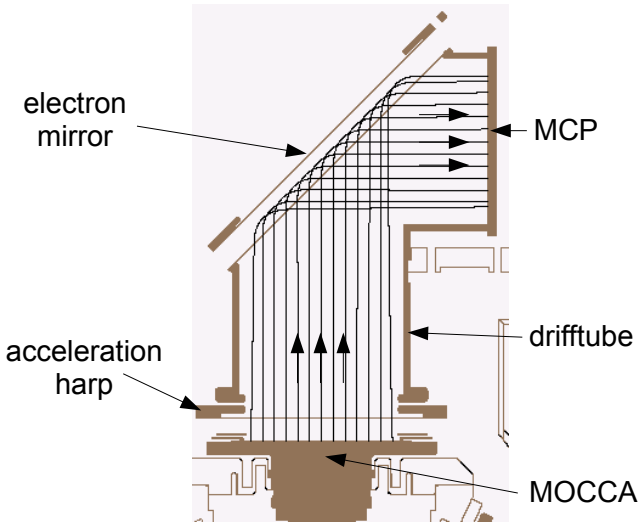

Figure 10: Picture of an ion-optical impression at a realistic model of the ETS. This realistic model will be described in further detail in section 4. Trajectories are displayed in black and are shown at the central cross section through the ETS. Electrons were started at normal incident to the detector surface with 0.1 eV kinetic energy. Typical electron trajectories will most likely differ from the shown trajectories due to initial polar angles and kinetic energies of electrons. The trajectories were calculated in the software package SIMION [6] by Newton's second law of motion in relativistic form. For this the electric field of the ETS was obtained by solving Laplace's equation with the applied potentials at the electrodes of the ETS as corresponding boundary conditions.

least one elementary charge $Q = e$, but most likely this amount of charge will be greater. Thus the maximum ratio of gravitational force F_g and electrostatic force F_e will be

$$\frac{F_\mathrm{g}}{F_\mathrm{e}} \propto 10^{-6} \quad , \tag{10}$$

and therefore it is legitimate to neglect gravity by earth when calculating the trajectories of electrons via eq. (7). The remaining electrostatic force $\mathbf{F}$ on the electrons is obtained by SIMION through calculation of the electric field $\mathbf{E}$ of the ETS:

$$\mathbf{F} = -e\mathbf{E} \quad . \tag{11}$$

The Maxwell-equations for the electric field in the case of electrostatics are:

$$\nabla \cdot \mathbf{E} = \frac{\rho}{\epsilon_0} \tag{12}$$

$$\nabla \times \mathbf{E} = \mathbf{0} \quad . \tag{13}$$

Here ρ is the spatial charge distribution. The second Maxwell-equation reveals the electric field as a conservative field. Thus the electric potential U at point $\mathbf{r}$ is given as the line integral along any arbitrary path from a reference point $\mathbf{r}^*$ to $\mathbf{r}$:

$$U(\mathbf{r}) = -\int_{\mathbf{r}^*}^{\mathbf{r}} \mathbf{E}(\mathbf{r}') \cdot \mathrm{d}\mathbf{l}' \quad . \tag{14}$$

In the accomplished simulations, the reference point $\mathbf{r}^*$ is on the surface of MOCCA, defining the ground potential as $U = 0\,\mathrm{V}$. If the potential is given, then the electric field may be obtained by

$$\mathbf{E} = -\nabla U \quad . \tag{15}$$

With eq. (12) a correlation is given between potential and spatial charge distribution, namely Poisson's equation:

$$\triangle U = -\frac{\rho}{\epsilon_0} \quad , \tag{16}$$

The charge which defines the potentials at the ETS is confined to the electrodes of the ETS. Secondary electrons move in the region between electrodes, where $\rho = 0\,\mathrm{C\,m^{-3}}$. For this region eq. (16) reduces to Laplace's equation:

$$\triangle U = 0 \quad . \tag{17}$$

This is the equation solved by SIMION in order to obtain the electric potential of the ETS and thus the electric field via eq. (15). The potentials applied on the electrodes of the ETS constitute as corresponding boundary conditions for the solution of this differential equation. SIMION uses the following method [11]: At point $\mathbf{r}$, the value $U(\mathbf{r})$ is the average value of U over a spherical surface A centered at $\mathbf{r}$ and with Radius R,

$$U(\mathbf{r}) = \frac{1}{4\pi R^2} \oint U \,\mathrm{d}A \quad . \tag{18}$$

simulated A grid of points is defined over the space in which the electric field is required. With the given boundary conditions, the potential on the corresponding boundary points is set. In several iteration loops eq. (14) is applied such that the electric potential of any point is estimated as the average potential of its nearest neighbor points, until the resulting values converge. Thus a numerical solution to Laplace's equation can be achieved [12].

3 Simulations Within a Simplified Model

Simulations of the ETS were accomplished in SIMION [6] in order to affirm the working principle of the ETS. The two main concerns are the conservation of timing information and the possibility of mapping between MOCCA and MCP, as stated in section 1.4. A first simulative approach was accomplished within a simplified model of the ETS and is described in this section. Confirmation of working principle of the ETS in the simplified case would give rise to the design of a realistic model of the ETS. This realistic model will be presented in section 4.

Within the simplified model, the concept of the ETS was divided into its two major components, namely the acceleration harp and the electron mirror. These two components were modeled separately in SIMION. This division intended to investigate the influence of each distinct component on the behavior of secondary electrons in the ETS. As stated in section 1.4, the ideal case would be that a projection of electron positions at MCP on MOCCA would exhibit no displacement between electron positions and corresponding fragment positions. Alone from the possible initial polar angles of secondary electrons such a displacement was most likely expected. This displacement will be called *electron displacement* or simply *displacement* if it is clear from the context.

In the simulation of the simplified model, a micro lensing effect was observed and will be discussed exemplary at the acceleration harp in section 3.1. This effect constituted as an origin to electron displacement in addition to the initial conditions of secondary electrons as described in section 2.1. Micro lensing also occurred at the wires of the electron mirror, but there the setting of wires was too complicated for a basic discussion. The contribution to the electron displacement due to micro lensing will be compared to the contribution due to initial conditions of electrons at the individual model of the acceleration harp in section 3.1. Qualitative approval and quantitative discussion of the electron mirror will be provided in section 3.2. The propagation of the electron displacement firstly at the acceleration harp and secondly at the electron mirror was examined as well. Simplifications, procedure, and results of the simulations of both components will be discussed in the following.

3.1 Electron Acceleration and Micro Lensing

It was intended to examine the influence of the acceleration harp on secondary electron behavior in the ETS. For this purpose a simplified model of the ETS was created in SIMION as shown in fig. 11. The origin of the model was set to the center of MOCCA. The electron mirror was excluded from this model, such that the distortion of ideal trajectories by the mirror was neglected and electron trajectories were not bent at all. In this model the shape of the drifttube was chosen to be rectangular because of simplicity of design in SIMION. At the opened sides of the rectangular drifttube the program extents the model towards infinity for calculation of electric potentials.

The dimensions of the simplified model shown in fig. 11 were chosen accordingly to the dimensions as intended for the real ETS at this stage of design of the ETS: MOCCA and MCP were modeled as squares of 50 mm length. The proper flight distance of electrons

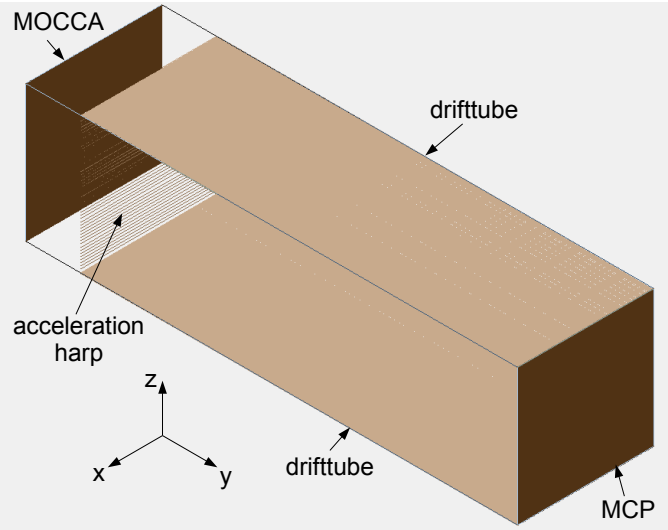

Figure 11: Picture of a simplified model of the ETS, including MOCCA, the acceleration harp, the drifttube, and the MCP. The electron mirror was excluded in order to study solely the influence of the acceleration harp on electron behavior. The drifttube was simplified to be rectangular in this model for designing reasons in SIMION. The dimensions of this model were chosen accordingly to the dimensions as intended for the real ETS at this current stage of design. The distance between MOCCA and MCP was fixed to 180 mm as the proper flight distance of electrons.

from MOCCA to MCP was fixed to 180 mm, as it would be the length of all trajectories of electrons starting at normal incident as indicated in fig. 5 in section 1.4. The distance d between MOCCA and the acceleration harp constituted as parameter in the accomplished simulations. In fig. 11, the model is shown for d = 20 mm. Increasing d shortened the length of the remaining drifttube since the distance between MOCCA and MCP was fixed. The spacing of the wires of the acceleration harp was w = 1 mm. The width of all plates and wires were modeled as infinitesimal small in SIMION, therefore they were treated as transparent for electrons in SIMION.

MOCCA constituted in all simulations as reference electrode of ground potential. For all simulations a voltage of 5 kV was applied on the acceleration harp, drifttube, and MCP. In order to get a first ion optical impression of this setting, electrons were started with normal incident towards MOCCA and were equidistantly spaced with 0.2 mm in z-direction. Their initial kinetic energy was 0.1 eV, which is negligibly small in comparison to the total energy gained in the acceleration. Resulting electron trajectories are shown exemplary at the five middle wires in fig. 12. Following the trajectories from left to right in fig. 12, it is observed that behind every wire a focal point occurred. Thus each wire of the harp constituted not only as an accelerator but also as a micro lens for the electrons. This effect is referred to as *micro lensing* and is expected to be encountered at every

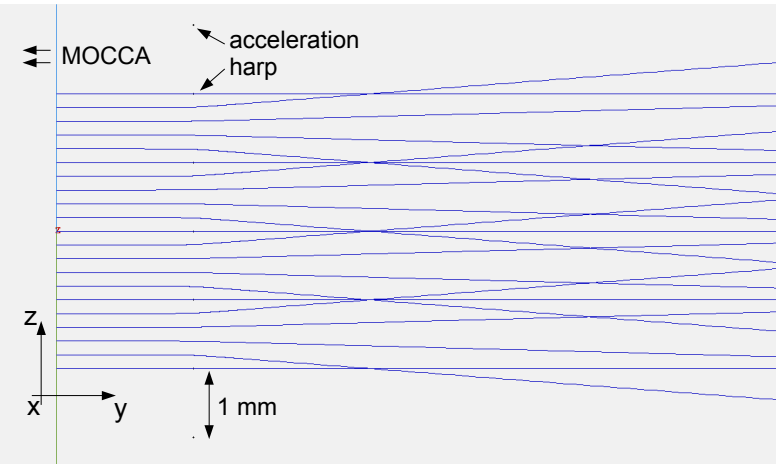

Figure 12: Picture of a first ion-optical impression at the acceleration harp in the simplified model of the ETS. Electron trajectories are drawn in blue. Electrons were started at normal incident towards MOCCA with a spacing of 0.2 mm and an initial kinetic energy of 0.1 eV. It is observed that focal points occurred behind each wire of the acceleration harp. This effect is referred to as *micro lensing* and is expected to be encountered at every electrostatic harp.

electrostatic harp passed by electrons.

The micro lensing can be understood by the potential energy surface view for the acceleration harp as shown in fig. 13. The wires constituted as points of lowest potential for the electrons. Their attractive force onto the electrons is represented by the negative slope of the ramp in the region between MOCCA and the acceleration harp. The hollows towards the wires gave rise to the micro lensing effect. Therefore each electron experienced a displacement

$$\Delta z = z_\mathrm{f} - z_\mathrm{i} \tag{19}$$

between final position at MCP and initial position at MOCCA in z-direction. This displacement was zero only when the electron was started with normal incident exactly at the z-position of a wire or in the center between two wires. A varying Δz may result in mixing the projected positions on the MCP detector. In turn, reducing the micro lensing would improve the possibility of mapping between MOCCA and MCP.

For this purpose two parameters were considered to influence the micro lensing: the distance d between MOCCA and the acceleration harp, and the spacing w of the wires of the acceleration harp. Changing both parameters at the same factor β would have scaled the potential energy surface shown in fig. 13 at this same factor β. Electrons with equal initial conditions would then have experienced the same gradient normal to the wires in the hollows near to the wires. Thus the electron displacement was expected to be dependent on the ratio $\mathrm{w/d}$.

An investigation of varying d at a constant w = 1 mm is shown in fig. 14. Electrons were started at normal incident in a line sequence in z-direction with initial kinetic energy of 0.1 eV. It was observed that increasing d led to decreased amplitudes of electron displacement Δz. Therefore it would be best to increase d as much as possible regarding electrons starting at normal incident. However, when considering realistic electron trajectories with initial polar angles of secondary electrons, there might be a regime in which increment of d would lead to a greater increment in electron displacement due to initial angles than the decrement of displacement due to micro lensing. Moreover, extending d towards the size of MOCCA would introduce strong boundary effects on the detector edges (field leaking).

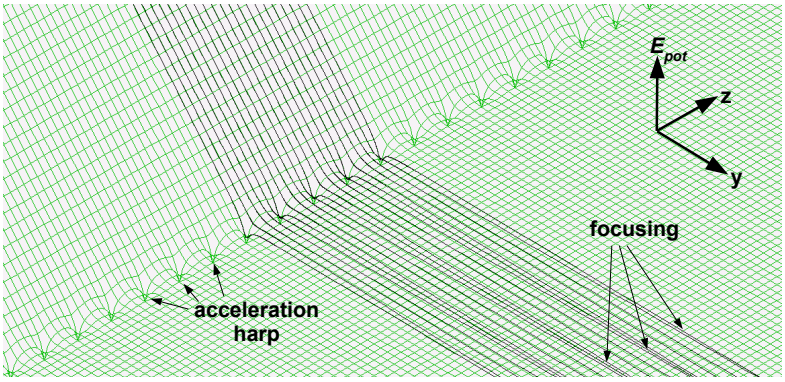

Figure 13: Picture of potential energy surface view for fig. 12. Here electron trajectories are drawn in black. The wires of the acceleration harp constituted as points of lowest potential, such that the hollows towards the wires gave rise to the micro lensing effect.

Another simulation intended to compare the contribution to electron displacement due to micro lensing with the contribution due to initial conditions of secondary electrons. This was done for a distance d = 10 mm between MOCCA and acceleration harp. The implementation of the initial conditions were realized as described in section 2.1. For the comparison of these contributions to the electron displacement, an investigation region at the acceleration harp was chosen for symmetry reasons: Looking from MOCCA towards the MCP and considering the potential energy surface view in fig. 13, the region between two wires was approximately equal at both, the left and right side of a specific wire. Inequalities may have arisen solely from the boundary conditions at the walls of the drifttube. Moreover, the region between two wires was approximately symmetrical when dividing it into halves. With a wire spacing of w = 1 mm, the region at the central wire between $z = 0.0$ mm and $z = 0.5$ mm normal to wires was therefore chosen as investigation region. The results from this region were expected to represent the remaining acceleration harp as well.

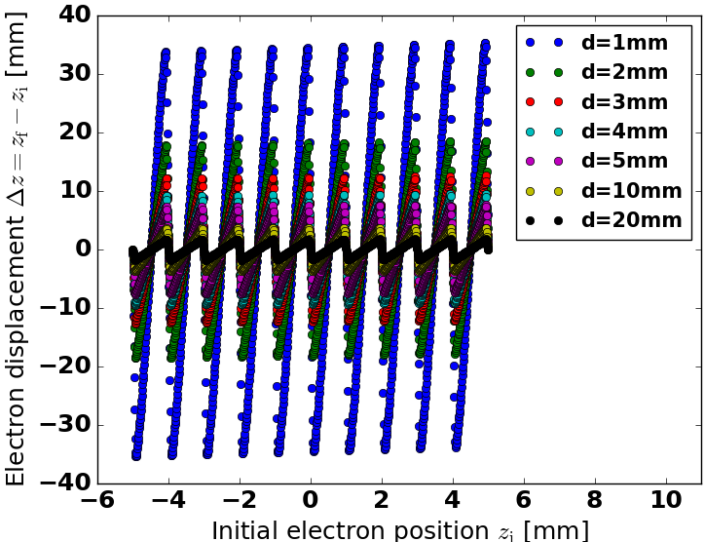

Figure 14: Plot of electron displacement due to micro lensing for different distances d between MOCCA and the acceleration harp at constant wire spacing w = 1 mm. Abscissa shows initial electron position z_i normal to the wires. Wires are placed at integer values of z. Ordinate shows the displacement $\Delta z = z_f - z_i$ between final and initial z-position due to micro lensing. It is concluded that d should be increased as much as possible for reducing the micro lensing effect in the case of electrons starting at normal incident.

Results of a Monte-Carlo simulation in this investigation region are shown in fig. 15. In the central cross section of the model in fig. 11, i.e. the plane $x = 0$, six equidistant initial positions z_i were chosen such that the smallest position was very close to, but not exactly at the central wire of the acceleration harp. This intended to reflect the real ETS, because the wires of the acceleration harp will be non-transparent for neutral fragments. Thus at positions exactly at the wires, most likely no secondary electrons would be produced at all. At each initial position z_i a number of N = 100 000 electrons were simulated. Each electron was simulated with unique random initial conditions, namely polar angle and kinetic energy, according to the implementation described in section 2.1.

The electron displacement was projected at two directions, namely the displacement

$$\Delta x = x_f - x_i = x_f \tag{20}$$

along the wires and the displacement Δz normal to the wires (cf. eq. (19)). The mean absolute displacement in both directions is shown for each initial electron position z_i

in fig. 15:

$$\overline{|\Delta x|} = \frac{1}{\mathrm{N}} \sum_{j=1}^{\mathrm{N}} \left| x_{\mathrm{f},j} - x_{\mathrm{i}} \right| \tag{21}$$

$$\overline{|\Delta z|} = \frac{1}{\mathrm{N}} \sum_{j=1}^{\mathrm{N}} \left| z_{\mathrm{f},j} - z_{\mathrm{i}} \right| \quad . \tag{22}$$

Error bars were calculated as $\sigma/\sqrt{\mathrm{N}}$ with standard deviation σ. The contribution to the mean displacement due to initial conditions of secondary electrons was assumed to be equal for both directions, because the p.d.f. for the azimuthal angle of secondary electrons is isotropic.

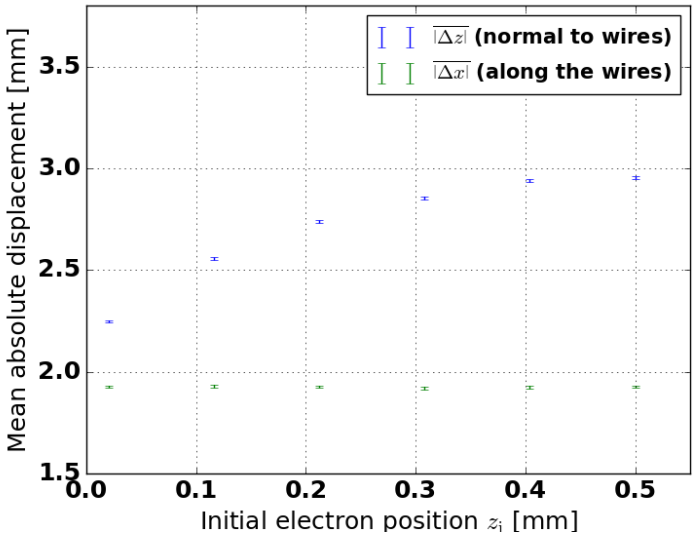

Figure 15: Results of a Monte-Carlo simulation of electron displacement at the center of the acceleration harp. Abscissa shows initial electron position z_{i} normal to wires in the plane $x = 0$. The wires of the acceleration harp had a spacing of $\mathrm{w} = 1\,\mathrm{mm}$ and were placed at integer z-values. $\mathrm{N} = 100\,000$ electrons were simulated with implemented initial conditions at each start position. Final electron positions at the MCP were recorded. Ordinate shows the mean absolute displacement $\overline{|\Delta x|}$ along the wires and $\overline{|\Delta z|}$ normal to the wires. Error bars are calculated as $\sigma/\sqrt{\mathrm{N}}$ with standard deviation σ. Since micro lensing occurred solely in z-direction, it was concluded that the contribution to electron displacement due to initial conditions is greater than the contribution due to micro lensing.

On the one hand, no micro lensing occurred along the wires, therefore the only contribution to the displacement Δx was due to the initial conditions of electrons. Because of that, the same mean absolute displacement $\overline{|\Delta x|}$ was expected for each initial position z_i. This was indeed found in fig. 15. On the other hand, because micro lensing occurred normal to the wires, the mean absolute displacement $\overline{|\Delta z|}$ was expected to differ from $\overline{|\Delta x|}$. Again, this was indeed found in fig. 15: The micro lensing increased the mean absolute displacement in z-direction. Moreover, a monotonic increment of $\overline{|\Delta z|}$ was observed for increasing z_i.

Subtracting $\overline{|\Delta x|}$ from $\overline{|\Delta z|}$, it was concluded that the contribution to the displacement by initial conditions was greater than the contribution by micro lensing, because micro lensing occurred solely in z-direction. This conclusion could be generalized from the described investigation region to the whole acceleration harp.

3.2 Electron Mirror and Further Analysis

It was intended to examine the influence of the electron mirror on secondary electron behavior in the ETS. For this purpose the results from the Monte-Carlo simulation presented in section 3.1 were implemented into a simulation of a simplified model of the electron mirror.

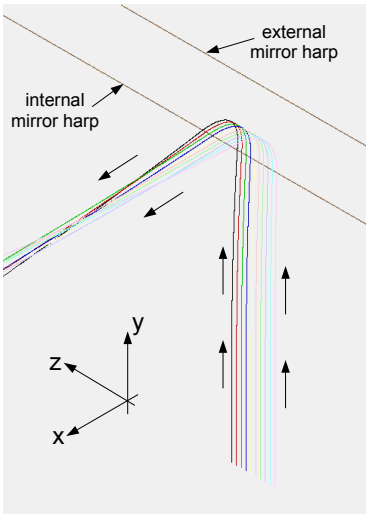

Figure 16: Picture of electron trajectories at the center of the simplified model of the electron mirror. Electrons were started in an equidistant line sequence with parallel velocities at normal incident. Initial kinetic energy of electrons was 5 keV, according to the acceleration voltage. Trajectories are highlighted in different colors. Micro lensing can be observed after the electrons have passed the mirror.

The mirror was modeled within SIMION as two rows of harps of the same kind and dimensions as the acceleration harp in section 3.1. Thus the wire spacing was set to $w = 1\,\text{mm}$ for each harp and the direction along the wires was extended towards infinity for calculation of electric potentials by SIMION. At the front mirror harp, where electrons were supposed to enter and exit the mirror, the voltage was set to $5\,\text{kV}$. At the back mirror harp the voltage was set to $-5\,\text{kV}$. This is an exception to the proposed application of $0\,\text{kV}$ in section 1.4, because this proposed value had been changed throughout the course of simulations. No qualitative changes are expected from this change. With the separation between the two harps set to $10\,\text{mm}$, the electrons experienced a mean gradient of $1\,\text{kV}\,\text{mm}^{-1}$ inside the mirror.

A first ion optical impression of this simplified model of the electron mirror is given in fig. 16. As expected, incoming electrons at normal incident were bent at 90°. However, micro lensing was observed for electrons having traversed the mirror. This was expected to worsen the contribution to electron displacements due to the mirror when compared to the contribution from the acceleration harp only. In order to examine this, the models of the acceleration harp and the electron mirror were combined as illustrated in fig. 17:

The Monte-Carlo simulation from section 3.1 was executed, but this time the positions and velocities of electrons were recorded at the plane $y = 52\,\text{mm}$. This recorded data was implemented as initial conditions of electrons in the simplified model of the mirror. Thus the propagation of electron displacement due to micro lensing firstly at the acceleration harp and secondly at the electron mirror was ensured. The remaining $64\,\text{mm} + 64\,\text{mm}$ complemented the proper flight distance of electrons.

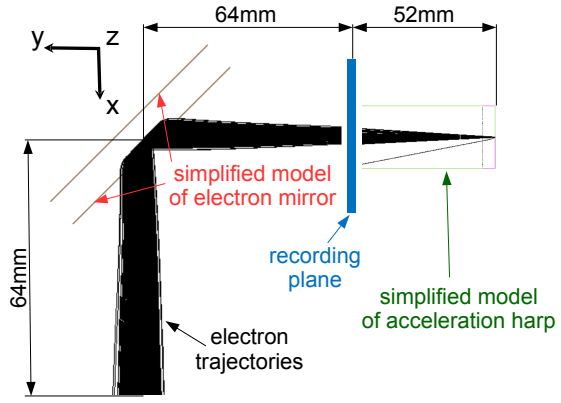

Figure 17: Picture of the simulative combination of simplified models of the acceleration harp and the electron mirror. The Monte-Carlo simulation from section 3.1 was executed and positions as well as velocities of electrons were recorded at the plane $y = 52\,\text{mm}$. This data constituted as initial conditions of simulated electrons in the model of the mirror. This way the propagation of electron displacement from one component of the ETS to the other was simulated.

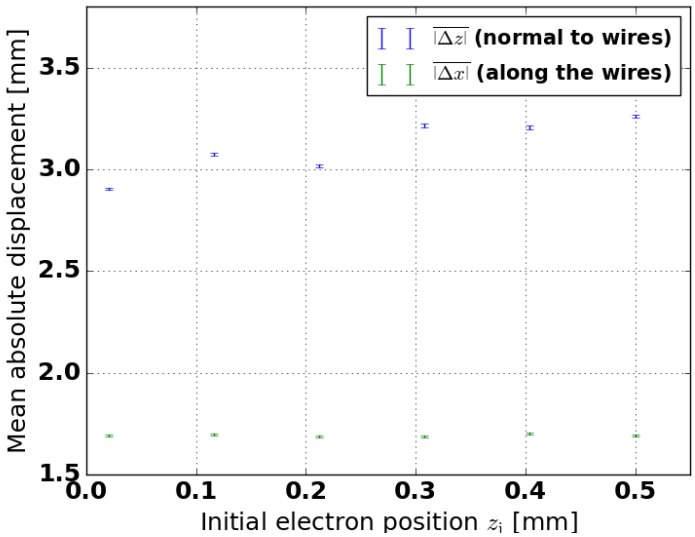

Figure 18: Results of a Monte-Carlo simulation of electron displacement at the center of the electron mirror. Further description of the simulative execution is provided in fig. 15 and fig. 17. In comparison to fig. 15, it is concluded that the electron displacement normal to the wires was increased by the influence of the electron mirror. However, the contribution to the displacement due to initial conditions was still greater than the contribution due to micro lensing.

The results of this procedure are shown in fig. 18. It was an unexpected result that the values of the mean electron displacement $\overline{|\Delta x|}$ along the wires in fig. 18 were not equal to but smaller than in fig. 15. Since along the wires no micro lensing occurred, only the initial conditions of electrons contributed to electron displacement along the wires. Hence the same electron displacement along the wires was expected for the model including the mirror when compared to the model excluding the mirror. It was assumed that this was a focusing effect of the electron mirror. Due to the finite dimensions of the harp wires, the potential lines along the wires formed a small gradient towards the center of the mirror. Thus the incident of 45° of incoming electrons favored this focusing, whereas this could not be observed at the acceleration harp because there the initial electron positions were in the central plane of the harp.

Again compared to fig. 15, it was observed that the mean absolute displacement $\overline{|\Delta z|}$ normal to the wires was greater than for the model with acceleration harp alone. This was expected since the electrons encountered another gradient normal to the wires due to micro lensing at the electron mirror. However, an electron might have experienced opposite directions of gradients, firstly at the acceleration harp and secondly at the electron mirror. E.g. the contribution to Δz might have been positive at the acceleration harp and negative at the electron mirror or vice versa. Therefore the mirror was assumed

to propagate the electron displacement not only by an increase of Δz but also by a decrease of Δz. The ratio of increment and decrement of Δz by this propagation was assumed to be dependent on the initial electron position z_i. This is indicated by the variation of increment of $\overline{|\Delta z|}$ in fig. 18 when compared to fig. 15. However, subtracting the mean electron displacements $\overline{|\Delta x|}$ and $\overline{|\Delta z|}$ from each other, it was still concluded that the contribution to the displacement due to initial conditions was greater than due to micro lensing.

Furthermore, the distribution of electron displacement was examined in order to estimate the possibility of mapping between MOCCA and MCP within the simplified models of the ETS. Projected at both directions, the distribution of electron displacement is shown in fig. 19 for the same data sample as in fig. 18, namely $\mathrm{N} = 100\,000$ electrons simulated each for six initial positions z_i. It is observed that the absolute displacement $|\Delta x|$ along the wires was distributed approximately equally for each initial electron position z_i. This was expected due to the absence of micro lensing in x-direction. The micro lensing in z-direction lead to small variations in the distributions of absolute displacement $|\Delta z|$ normal to the wires, but the general shape was not affected.

For both directions the number of counted electrons monotonically decreased with increasing electron displacement, thus small displacements were more likely than great displacements. This decrement was stronger along the wires and more electrons were counted for $|\Delta x| \leq 2\,\mathrm{mm}$ than for $|\Delta z| \leq 2\,\mathrm{mm}$. Furthermore, for both directions the number of electrons with a displacement greater than 8 mm was negligibly small. Compared to the length of approximately 45 mm of the squarish detection area of MOCCA, it was therefore concluded that a mapping process between secondary electrons at MCP and fragments at MOCCA would have been likely possible within the simplifications of the modeled ETS. This was restricted by sufficient large distances between the impinged fragments. For a typical event, minimal distances of fragments in the regime of 3.4 mm along the wires and 6.6 mm normal to wires would have been expected to lead to a successful assignment in most cases. These values were estimated as twice the maximum mean absolute displacement of electrons from fig. 18.

Moreover, the distribution of TOF of electrons was examined in order to judge whether the timing information of fragments are conserved by secondary electrons within the simplified models of the ETS. This distribution of electron TOF is shown in fig. 20. Firstly, the distribution of TOF was found to be similar for each initial position. Secondly, almost all electrons had a TOF in the range of 4.54 ns to 4.59 ns. From this it is concluded that neither the micro lensing nor the initial conditions of secondary electrons had a major influence on the TOF. Furthermore, this affirmed the conservation of timing information within the simplified model of the ETS, because the variance in electron TOF was small compared to the typical relative timing difference of $\lesssim 100\,\mathrm{ns}$ between fragments (cf. section 1.2).

As a result from simulations within a simplified model, the working principle of the ETS could be affirmed. This gave rise to the design of a realistic model of the ETS, in order to reaffirm the working principle of the ETS under realistic conditions. This will be discussed in the following section, using the knowledge gained from this section.

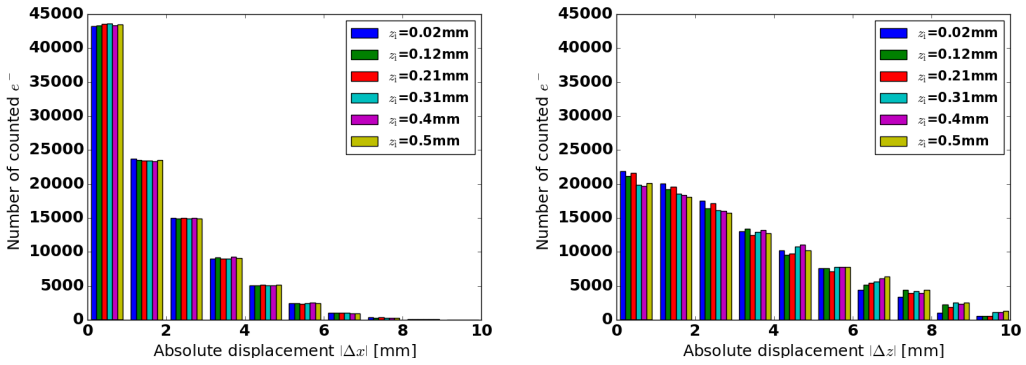

(a) (b)

Figure 19: Plots of distribution of electron displacement for the same data sample as in fig. 18.
a) Distribution of absolute displacement $|\Delta x|$ along the wires.
b) Distribution of absolute displacement $|\Delta z|$ normal to wires.
In both cases the shape of distribution was found to be similar for each initial position z_i. It is observed that small displacements showed a higher probability than great displacements. Compared to the approximately $45 \times 45\text{mm}^2$ squarish detection area of MOCCA, mapping between MOCCA and MCP within the simplified model of the ETS would be likely possible under restriction of sufficient large distances between impinged fragments.

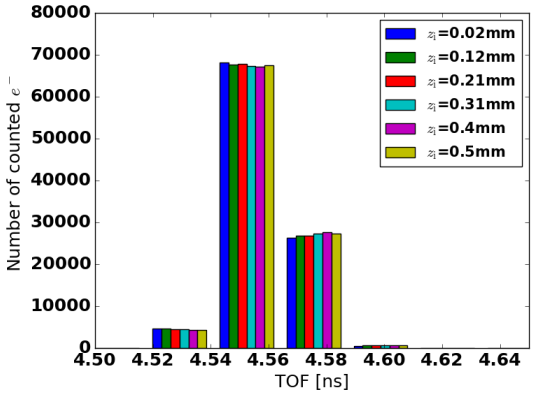

Figure 20: Plot of distribution of electron TOF for the same data sample as in fig. 18. The variance in TOF of all simulated electrons was found to be small compared to the typical timing difference of $\lesssim 100\,\text{ns}$ between fragments. Thus the conservation of timing information by secondary electrons was affirmed within the simplified model of the ETS.

4 Analysis of a Realistic Electron Transport System

The working principle of the ETS has been affirmed in section 3 within simulations at a simplified model of the ETS. Intending to test a realistic model of the ETS next, a CAD-model was designed in the CAD software Solid Edge (Siemens PLM Software) [13] and was imported into SIMION. Simulations at this CAD-model were supposed to reaffirm the working principle of the ETS under more realistic conditions than the simplifications of the model in section 3. As stated in section 1.4, the main aspects were firstly the conservation of timing information of fragments by secondary electrons, and secondly the possibility of a mapping process between electrons at MCP and fragments at MOCCA. Throughout the investigation of realistic models of the ETS, there have been created and tested several versions of CAD-models. The latest version (effective date: Feb. 2018) is shown in fig. 21.

The general setting was implemented as proposed in section 1.4. The dimensions of this model are given in fig. 22, where the central cross section of the model is shown after import into SIMION. The detection area of MOCCA was given by a square-shaped chip

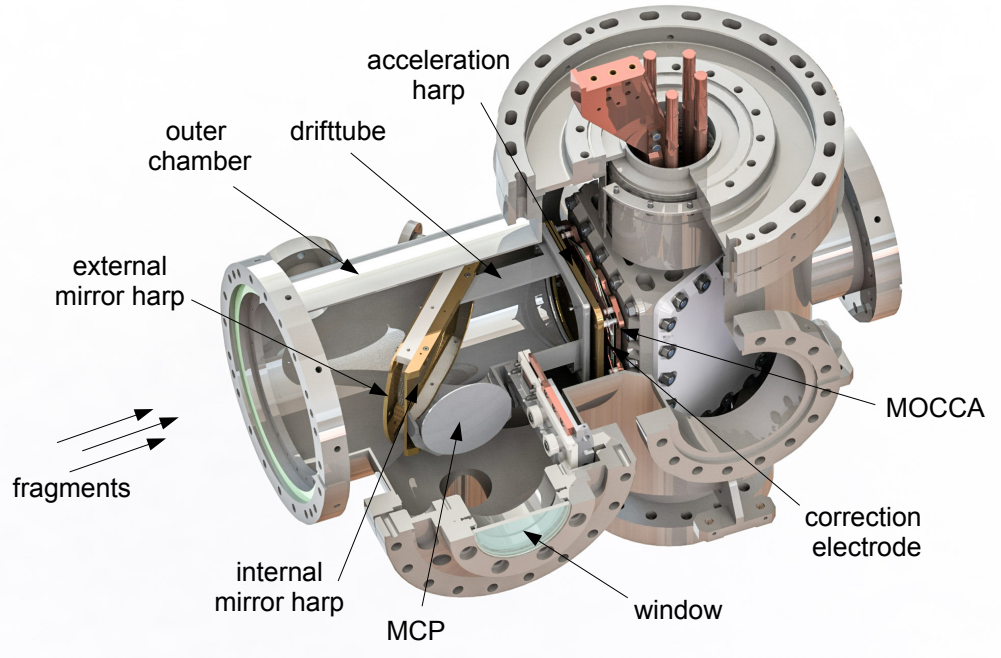

Figure 21: Image of a realistic CAD-model of the ETS. The model was designed with the software Solid Edge and was imported into SIMION. It was the latest version (effective date: Feb. 2018) of a series of CAD-models that have been tested in simulations. Image courtesy of Mr. Ruben Kankanyan from MPIK.

of approximately $45 \times 45\text{mm}^2$ size. The detector chip is mounted to the underlying copper base plate by a metallic frame, which extends above the detector surface by 1.4 mm. Additionally to the original concept, a flat thin electrode consisting of a quadratic aperture exactly matching the detection area of MOCCA was implemented parallel to the surface of MOCCA. Its purpose is to generate a correction field in order to compensate for the edge effects due to the non-flat detector holder. These edge effects would otherwise have affected the electron trajectories in an unintended way. Motivation for this correction electrode will be given in section 4.1. Like the acceleration harp, the harps of the electron mirror had a wire spacing of $w = 0.7\,\text{mm}$. The wires of all harps were treated as transparent for electrons in all simulations presented in this section.

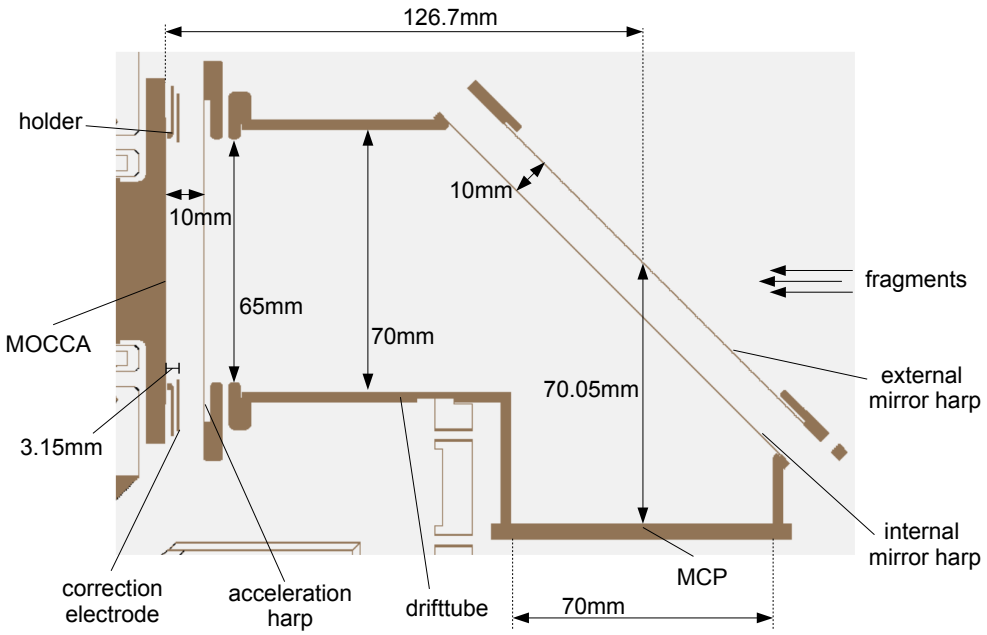

Figure 22: Picture of the CAD-model from fig. 21 imported into SIMION. Shown is the central cross section through the modeled ETS. In addition to that, dimensions of the model are given.

When importing the CAD-model into SIMION, the model was divided into cubic pixels for calculation of electric potentials. The higher the resolution of pixels was, the higher was the enabled precision of calculation. For memory allocation reasons, SIMION is limited with a maximum number of pixels for resolution of imported models. In order to achieve the best precision of calculation, the mirror symmetry of the ETS was used and solely the region indicated in fig. 23 of the CAD-model was imported. A resolution of $2811 \times 894 \times 2689 = 6\,757\,548\,426$ pixels of $0.1 \times 0.1 \times 0.1\text{mm}^3$ size was achieved. After

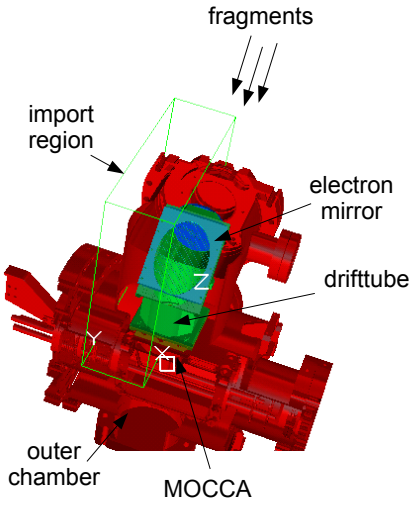

Figure 23: Picture of the region of the CAD-model imported into SIMION. Because SIMION is limited with a maximum number of pixels for resolution of imported models, the mirror symmetry of the ETS was used and only the indicated region (green cuboid) was imported. After import, this half was mirrored by SIMION in order to have a complemented model of the ETS. The non-imported parts are far enough from the ETS core region and are not expected to have any significant field contribution.

the import, SIMION was capable of mirroring this half of the model in order to have a complemented model for simulations. In the following, the analysis of this imported CAD-model of the ETS will be presented.

Before further analysis was possible, the above mentioned correction electrode needed to be implemented into the model. Reasoning for that will be given in section 4.1. Afterwards, analysis of behavior of secondary electron with start positions over the whole detection area of MOCCA will be provided in form of a Monte-Carlo simulation in section 4.2. The major concerns are firstly conservation of timing information, and secondly electron displacement for the mapping between MOCCA and MCP.

4.1 Correction Electrode

As already stated above, several version of the ETS CAD model have been created and tested. In these tests, trajectories of electrons with start positions over the whole detection area of MOCCA were simulated. Initial conditions of electrons were implemented as described in section 2.1. When the first version was tested, unexpected great displacements were observed for electrons starting near the edge of the detection area. These edge effects were observed to be the stronger the closer electrons were started to the edge. Trajectories of the extreme cases in which electrons were started in the four corners of the

detection area are shown in fig. 24a. The trajectories from all four corners were observed to mix for the most part at the center of the MCP. In contrast to that, edge effects were compensated in the latest version of ETS-models and resulting electron trajectories are shown in fig. 24b, where the electron positions where chosen similarly to fig. 24a. Here the electron displacements were sufficient low in accordance to the expected working principle of the ETS as described in section 1.4, such that no mixing of spatial electron distributions occurred.

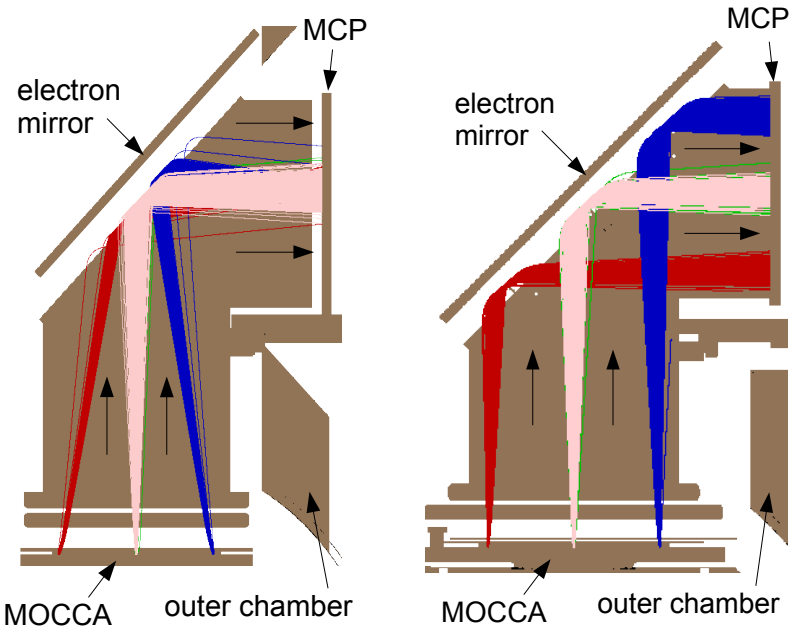

(a) (b)

Figure 24: Pictures of trajectories of electrons with initial positions at the four corners of the detection area of MOCCA. This is shown for different versions of CAD-models of the ETS: a) the first version without correction electrode and b) the latest version including the correction electrode at a potential of 1.575 kV. Each displayed trajectory color represents one of the four corners at which electrons were started.
a) The electrons encountered edge effects, giving rise to great electron displacements.
b) These edge effects were compensated, giving rise to sufficient low electron displacements in accordance to the expected working principle of the ETS.

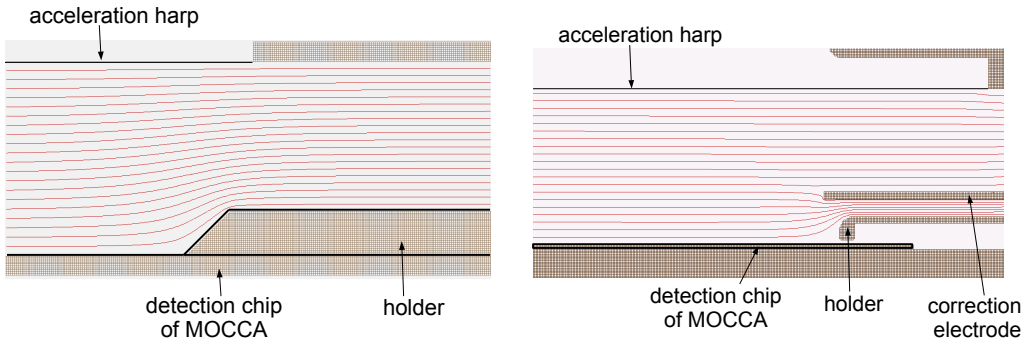

Figure 25: Pictures of potential lines near to the holder of the detection chip of MOCCA. This is shown for different versions of CAD-models of the ETS: a) the first version and b) the latest version. The 20 potential lines drawn in red are equidistant between 0 kV and 5 kV.
a) The edge effects could be understood by the potential lines which gave rise to gradients parallel to the detection area.
b) These edge effects were successfully compensated by implementation of a correction electrode at 1.575 kV.

The edge effects that occurred in the first version were traced back to the holder of the detection chip of MOCCA. In fig. 25a the potential lines giving rise to the edge effects are shown. The closer an electron was started to the holder, the greater was the gradient parallel to the detection area, giving rise to great displacements as shown in fig. 24a. This unintended affection of the holder on the secondary electrons had not been foreseen when this first CAD-model was created.

As it is inevitable to secure the detection chip of MOCCA with the holder, a compensation of edge effects was necessary. Otherwise the region of the detection area of MOCCA close to the edge would be useless considering the ability of mapping between MOCCA and MCP because of too large electron displacement. For this purpose a correction electrode has been implemented in all subsequent versions of CAD-models and was placed between MOCCA and the acceleration harp.

For the latest version, the successful compensation of edge effects is indicated by the potential lines shown in fig. 25b. It is observed that gradients parallel to the detection area are strongly reduced when compared to fig. 25a. This gave rise to electron trajectories already shown in fig. 24b. Note that the design of the holder changed, but that similar edge effects would have occurred without correction electrode. The dimensions of this electrode has already been described above in the introductory part of section 4. The correction voltage U_c to be applied on the correction electrode was firstly guessed as

$$U_c = \frac{d_c}{d_a} \cdot U_a = \frac{3.15\,\text{mm}}{10\,\text{mm}} \cdot 5\,\text{kV} = 1.575\,\text{kV} \quad . \tag{23}$$

Here d_c is the distance between MOCCA and correction electrode, d_a is the distance between MOCCA and acceleration harp, and U_a is the potential applied on the acceleration harp. When the estimated potential of $U_c = 1.575\,\mathrm{kV}$ was applied on the correction electrode at simulations of the latest version of the CAD-model, small edge effects were still noticed for evaluation of the electron displacement. This correction potential U_c was therefore kept as an adjustment parameter in order to minimize such edge effects. After the issue of correcting the electric field of the ETS near to the holder of MOCCA had been solved, further investigation of the ETS was performed by simulation of electron trajectories at this latest version of the CAD-model. For this simulation presented in the following, a correction voltage of $U_c = 1.77\,\mathrm{kV}$ was chosen, because this showed the smallest edge effects.

4.2 Main Analysis

In this section the main analysis of the latest version of realistic models of the ETS is presented. The method of evaluating the accomplished simulation will be described in section 4.2.1. Considering the timing information, the distribution of TOF of electrons will be discussed in section 4.2.2. Considering the possibility of mapping, the electron displacement will be discussed in section 4.2.3. The realistic model has already been described in the introductory part of section 4.

4.2.1 Evaluation Method for Monte-Carlo Simulation

A Monte-Carlo simulation of electron trajectories in the realistic model of the ETS was accomplished. The concepts of this simulation and the method of its evaluation is visualized in fig. 26. It was intended to investigate the complete detection area of MOCCA in order to give insight in the behavior of secondary electrons possibly induced anywhere at this area.

For this purpose a grid of start positions for electrons was defined over the detection area, which is schematically shown in fig. 26a. This grid was aligned along the wires of the acceleration harp. The spacing of the points of this grid was 0.35 mm in both directions, normal to and along the wires. This gave rise to 20 137 points of initial positions for secondary electrons. At each point $N = 1000$ electrons were simulated with initial conditions implemented as described in section 2.1. Thus a total number of 20 137 000 trajectories of secondary electrons was calculated within this Monte-Carlo simulation. For each electron the initial position, final position, and TOF was recorded. This data was evaluated as follows:

The distribution of recorded TOF values was already sufficient for consideration of conservation of timing information. It remained to examine the electron displacement. For this purpose, the final positions of all electrons which arrived at the MCP were projected on the plane of the detection area of MOCCA. This is illustrated in fig. 26b. Looking along the axis of incoming fragments with the MCP to the right hand, this projected situation is visualized in fig. 26c. The orientation at this projection is given by the alignment along the acceleration harp, similar to the grid of defined start positions in

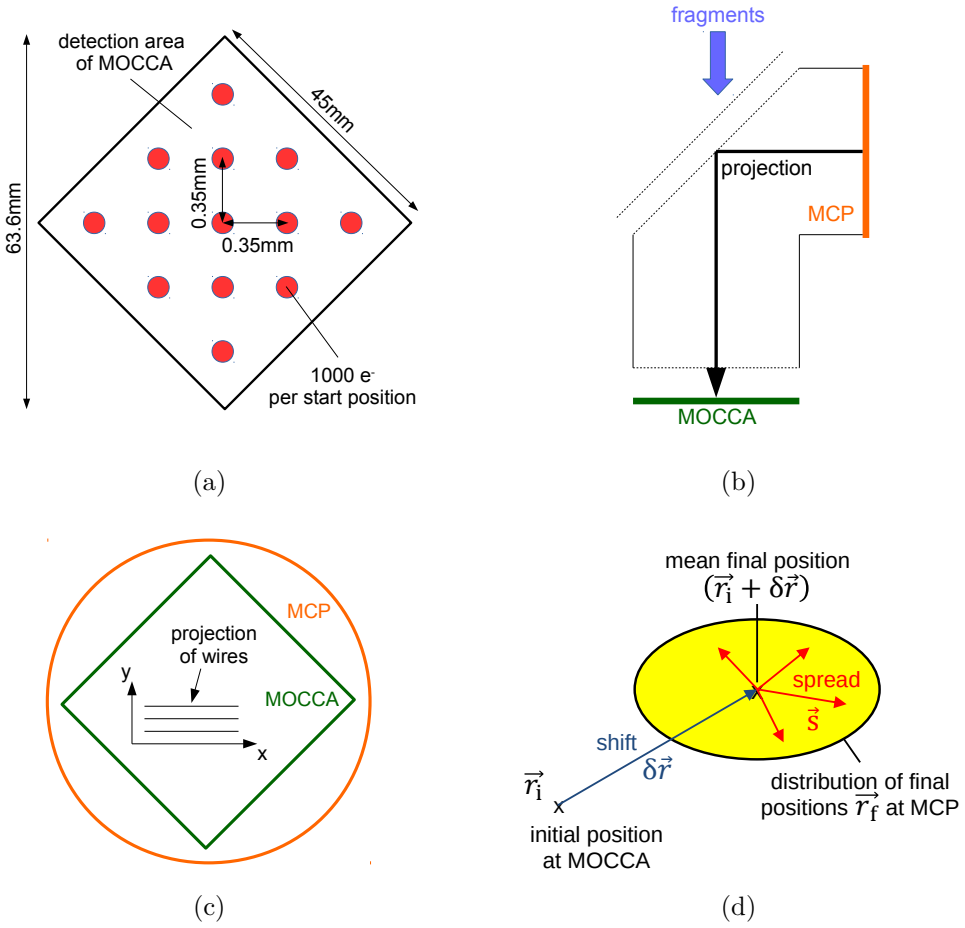

Figure 26: Illustrations of evaluation method of accomplished Monte-Carlo simulation.
a) A grid of start positions for electrons at the detection area of MOCCA was defined. Note that this scheme is not in scale. For visualization reasons only a few start positions are shown. In fact this definition of the grid with a spacing of 0.35 mm between the points gave rise to 20 137 points. For each point N = 1000 electrons were simulated.
b) The final positions of electrons at MCP were projected into the plane of the detection area of MOCCA, such that both detection areas of MCP and MOCCA would share the same center.
c) Perspective of the projection in b) when looking along the blue arrow in b). The orientation in this view is given by the two directions x, along the wires, and y, normal to wires of the acceleration harp. The wires are indicated by the black parallel stripes.
d) In the view of c), the electron displacement was divided into two quantities, namely shift and spread. Their definitions are mathematically given in the text.

fig. 26a. Thus the two directions of interest were x, the direction along the wires, and y, the direction normal to the wires, with corresponding unit vectors $\mathbf{e}_x$ and $\mathbf{e}_y$. The origin was set to the common center of MOCCA and MCP in this view. A general electron position with respect to the center of MOCCA or MCP was now given by

$$\mathbf{r} = x\mathbf{e}_x + y\mathbf{e}_y \quad . \tag{24}$$

The initial electron position at MOCCA is denoted with $\mathbf{r_i}$, the final electron position at MCP as $\mathbf{r_f}$. The mean final position, i.e. the centroid of the spatial electron distribution for electrons from one initial position, was calculated as:

$$\overline{x_\mathrm{f}} = \frac{1}{\mathrm{N}} \sum_{j=1}^{\mathrm{N}} x_{\mathrm{f},j} \tag{25}$$

$$\overline{y_\mathrm{f}} = \frac{1}{\mathrm{N}} \sum_{j=1}^{\mathrm{N}} y_{\mathrm{f},j} \quad . \tag{26}$$

A division of the electron displacement into the two quantities *shift* and *spread* gives rise to a quantification of the centroid and the size of each spatial electron distribution at MCP, as illustrated in fig. 26d. For given initial electron position, the shift is defined as the components of the vector from the initial position to the mean final position:

$$\delta x := \overline{x_\mathrm{f}} - x_\mathrm{i} \tag{27}$$

$$\delta y := \overline{y_\mathrm{f}} - y_\mathrm{i} \quad . \tag{28}$$

The spread is then defined as the mean length of all vectors from the mean final position to each individual final position, projected in both directions:

$$\mathrm{s}_x := \frac{1}{\mathrm{N}} \sum_{j=1}^{\mathrm{N}} \left| x_{\mathrm{f},j} - \overline{x_\mathrm{f}} \right| \tag{29}$$

$$\mathrm{s}_y := \frac{1}{\mathrm{N}} \sum_{j=1}^{\mathrm{N}} \left| y_{\mathrm{f},j} - \overline{y_\mathrm{f}} \right| \quad . \tag{30}$$

Additionally for a single electron, the length of the vector from the mean final position to the individual final position of this electron, projected in both directions, was called *singular spread*:

$$\sigma_x = |x_\mathrm{f} - \overline{x_\mathrm{f}}| \tag{31}$$

$$\sigma_y = |y_\mathrm{f} - \overline{y_\mathrm{f}}| \quad . \tag{32}$$

Therefore the spread in eq. (29) and eq. (30) could also be expressed with the singular spread:

$$\mathrm{s}_x = \frac{1}{\mathrm{N}} \sum_{j=1}^{\mathrm{N}} \sigma_{x,j} \tag{33}$$

$$\mathrm{s}_y = \frac{1}{\mathrm{N}} \sum_{j=1}^{\mathrm{N}} \sigma_{y,j} \quad . \tag{34}$$

The results of the evaluation of the accomplished Monte-Carlo simulation with the just described method is presented in the following.

4.2.2 Transmittance and TOF

On their guided way through the ETS, simulated secondary electrons may not have reached the MCP but impinged on a different electrode of the ETS. Those electrons would have given rise to a loss of timing information of fragments. Thus it was a concern to examine for every start position the fraction of electrons which reached the MCP. This is the transmittance of the ETS for secondary electrons. In the real ETS, electrons may also impinge on the wires of acceleration harp and electron mirror. Within the realistic ETS model, these wires had a width of only one pixel and were therefore modeled as transparent for electrons in SIMION. This was chosen because the high spatial resolution of the calculated electric field was preferred over the non-transparency. Thus the loss of timing information due to electron impingement on the wires was not included in this investigation of the transmittance.

The transmittance of the ETS for each start position at the detection area of MOCCA is shown in fig. 27a. Most of the detection area exhibited a transmittance of 100 %. Only at the four corners of the detection area the transmittance was reduced to lowest 80 %. This reduction was reasonable, because here the electrons were closest to the drifttube and therefore had the highest probability to impinge onto it. The dimensions shown in fig. 22 and fig. 26a clarify this: The acceleration harp had an opening diameter of 65 mm, the drifttube had a diameter of 70 mm, and the diagonal of the detection area of MOCCA had a length of 63.6 mm.

Furthermore, the asymmetry of reduction might have been a result from micro lensing (cf. section 3.1): The electron bending in y-direction might have given rise to a more likely impingement of electrons on the drifttube for the upper and lower corner than for the lefter and righter corner. From the transmittance shown in fig. 27a, it was concluded within this realistic model of the ETS that almost every secondary electron produced at MOCCA would be able to reach the MCP and would therefore be capable of transferring the timing information of fragments.

For the conservation of timing information of fragments, secondary electrons would need to have a small variance in TOF compared to the fragment impact-time difference within one dissociation event, as described in section 1.4. The distribution of recorded TOF of simulated electrons is shown in fig. 27b. Included are all simulated electrons over the detection area minus lost electrons due to non-perfect transmittance of the ETS. It was observed that most electrons had a TOF in the range of 4.945 ns to 4.975 ns within the FWHM read off as 30 ps. This FWHM is negligibly small compared to the difference between arrival times of fragments in the regime of $\lesssim 100$ ns. It was therefore concluded from this Monte-Carlo simulation that the realistic model of the ETS was capable of guiding the secondary electrons such that the timing information of fragments would be conserved.

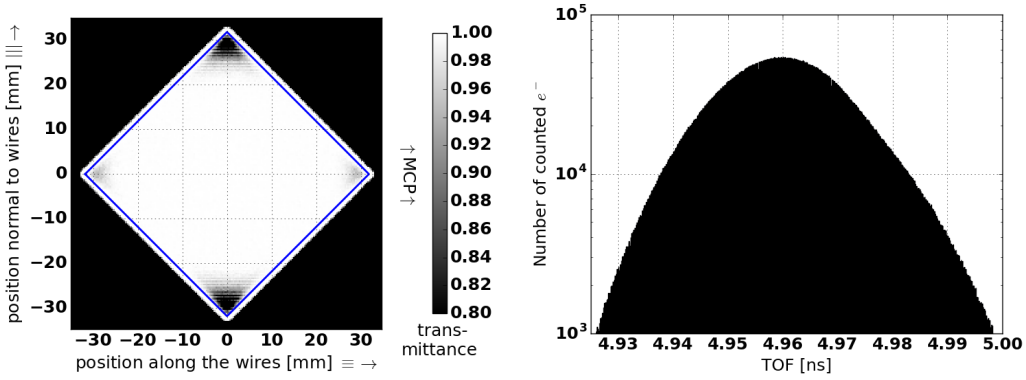

(a) (b)

Figure 27: a) Plot of the transmittance of the ETS for secondary electrons. For each point at MOCCA the fraction is shown of how many of the 1000 simulated electrons per point arrived at the MCP. The detection area is indicated by the blue square. Most of the points showed 100 % transmittance. Only at the corners of the detection area of MOCCA small regions with transmittance of lowest 80 % were observed. Thus it was expected that most secondary electrons induced by fragments at MOCCA would be able reach the MCP and would therefore enable timing measurement in this realistic model of the ETS. b) Picture of distribution of secondary electron TOF. Note the log-scale of the ordinate in this graph. The distribution includes all electrons that arrived at the MCP, regardless of their start position at MOCCA. The FWHM was read off as 30 ps, thus the timing information of fragments was expected to be conserved in this realistic model of the ETS, because this FWHM is negligibly small compared to the typical fragment impact-time difference within one dissociation event of $\lesssim 100$ ns.

4.2.3 Shift and Spread

Last but not least the ability of mapping between MCP and MOCCA was considered within the realistic model of the ETS. For this purpose the electron displacement was evaluated in form of the two quantities, shift and spread, as defined in section 4.2.1.

The shift is shown in fig. 28, projected in x- and y-direction. The positive shift for positive regions and the negative shift for negative regions, respectively, indicated that electrons were defocused towards the walls of the drifttube. This could be understood by looking at the apertures of the acceleration harp and the electron mirror:

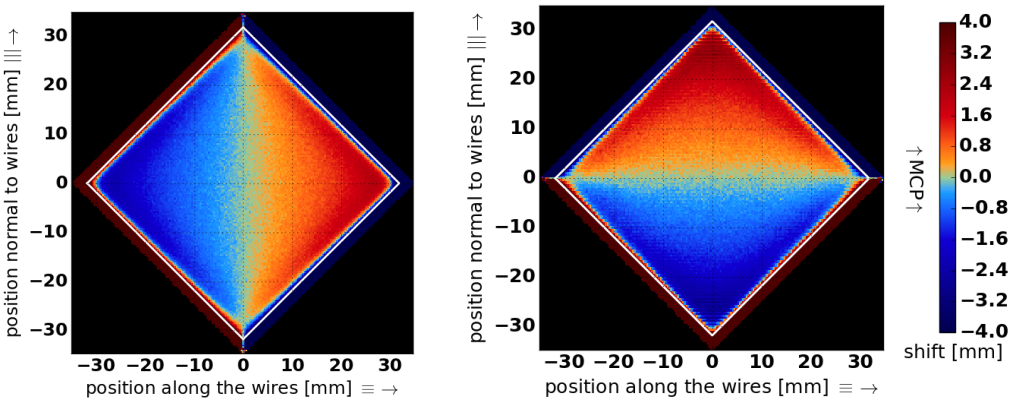

(a) (b)

Figure 28: Plots of the secondary electron shift projected as a) δx along the wires and b) δy normal to the wires. The detection area of MOCCA is indicated by the white square. The sign of the shift indicated that the electrons were defocused. Most points showed an absolute shift of below 2.0 mm. Only at the corners of the detection area of MOCCA an absolute shift greater than 2.0 mm could be observed. Except for regions close to the edge of the detection area, the shift monotonically increased in both directions. Thus in this realistic model of the ETS, the centroids of spatial secondary electron distributions were expected to not be mixed at the MCP when compared to the initial fragment positions at MOCCA (cf. fig. 6b).

If the drifttube had been completely closed, it would have formed a Faraday cage and would therefore have been a region of zero electric field. However, the apertures allowed the potentials of the outer chamber to effect the potentials in the inner of the drifttube in such a way that a gradient might have been established towards the walls of the drifttube. Most points of the detection area showed a shift lower than 2.0 mm in amplitude. Solely at the corners of the detection area a shift of greater amplitude was observed. The maximum shift was read off as approximately $\delta x_{\max} \approx 2.5\,\text{mm}$ and $\delta y_{\max} \approx 3.0\,\text{mm}$.

Moreover, the shift was revealed to monotonically increase in both directions. This increment was solely perturbed at the edges of the detection area. That perturbation was interpreted as an artifact from the edge effects (cf. section 4.1). From the monotonic increment of shift in both directions it was concluded that no mixing of spatial electron distributions took place, as indicated in fig. 6b in section 1.4. The overall defocussing should not affect the spatial assignment of MCP-impacted electrons to the MOCCA-impacted molecular fragments. It remained the question of overlap of these distributions as indicated in fig. 6a.

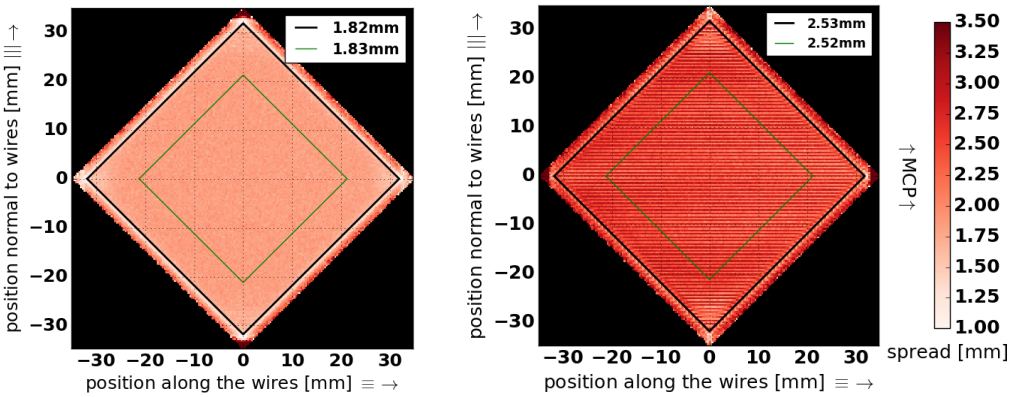

(a) (b)

Figure 29: Plots of the secondary electron spread projected as a) s_x along the wires and b) s_y normal to the wires. The detection area of MOCCA is indicated by the black square. The sub-structure in b) could be understood by the micro lensing as described in section 3.1. In contrast to that, the spread in a) had a negligibly small variance. The spread showed amplitudes lower than 3.0 mm for a) and lower than 2.0 mm for b). In addition to that, mean values of the spread over the whole detector area and the central detector area (green square of $30 \times 30\text{mm}^2$) are given.

The spread is shown in fig. 29, projected in x- and y-direction. In y-direction the spread showed a sub-structure. This could be understood by the micro lensing as described in section 3.1. In x-direction the spread was almost the same for every point. The mean spread over the detection area was evaluated as $\overline{s_x} = 1.82\,\text{mm}$ and $\overline{s_y} = 2.53\,\text{mm}$. These values were not influenced significantly by the edge effects. As all possible azimuthal angles for a secondary electron had the same probability, the spatial electron distribution on the MCP could have been expected to exhibit a circular shape. But because of the micro lensing normal to the wires, the spread was greater in y-direction than in x-direction (cf. section 3). Thus the spatial electron distribution was expected to be deformed into an elliptical shape.

Considering the question of overlap of spatial electron distributions, it was intended to characterize typical dimensions of such a distribution. For this purpose the distribution of the singular spread of all simulated electrons over the whole detection area, minus lost electrons due to non-perfect transmittance of the ETS, is shown in fig. 30. It was observed for both directions that the probability decreased monotonically towards high singular spread values. This shape of distribution did not change significantly over the detection area. Moreover, the HWHM was read off for both distributions and was found to be lower than or equal to the mean spread value as evaluated in fig. 29. From the distributions of singular spread it was concluded that the dimensions of spatial secondary

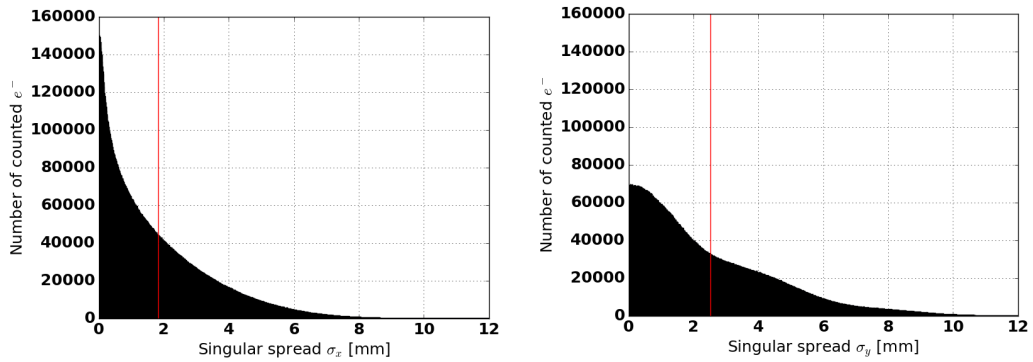

(a) (b)

Figure 30: Plots of distribution of the secondary electron singular spread projected as a) σ_x along the wires and b) σ_y normal to wires. These distributions include all simulated electrons started at MOCCA, regardless of their start position, minus lost electrons due to non-perfect transmittance of the ETS. The distribution shape did not change significantly across the detection area. Mean values over the detection area as evaluated in fig. 29 are indicated by the red lines.

electron distributions at MCP could be characterized for each point at MOCCA by the spread values in fig. 29. Furthermore, averaging over the whole detection area, dimensions of a typical spatial distribution could be approximated with the mean spread values.

For each point at MOCCA, the spatial electron distributions at MCP were imagined as ellipses with the spread values as semi-axes, as illustrated in fig. 31. These ellipses would have constituted as regions of likely final electron position, but of course a possible final electron position outside an ellipse would had non-zero probability due to the distribution of singular spread in fig. 30. Averaging over the the whole detection area, typical spatial distributions of all points were approximated as ellipses of same size, namely with the mean spread values as semi-axes. If the distance between two fragments at MOCCA had exceeded twice the mean spread values, i.e. $2\,\overline{s_x} = 3.64\,\text{mm}$ in x-direction and $2\,\overline{s_y} = 5.06\,\text{mm}$ in y-direction, the typical spatial electron distributions of these fragments would not have overlapped.

These distances were acceptable compared to the $44.8\,\text{mm} \times 44.8\,\text{mm}$ detection area of MOCCA [4], thus allowing for a good relative spatial resolution. For these distances the shift in fig. 28 showed differences in amplitudes that could have minor influence on these estimates. However, the defocusing of electrons would have given rise to a less likely overlap of spatial electron distributions. Therefore a successful mapping between MOCCA and MCP is expected under these restrictions of distance between fragments within this realistic model of the ETS. An even safer approximation could be drawn from the maximum spread values instead the mean spread values.

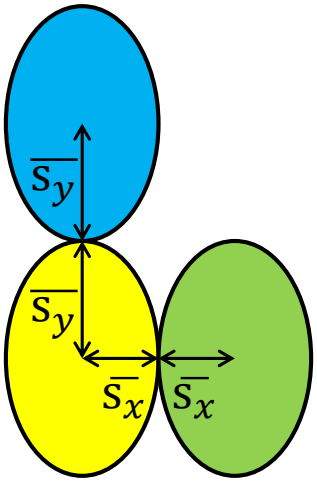

Figure 31: Scheme of typical spatial electron distributions at MCP due to three possible fragment positions at MOCCA. If the distance between fragments would exceed twice the mean spread values, a correct assignment of secondary electrons to their inducing fragments would have been likely within this realistic model of the ETS.

5 Conclusion and Outlook

In this thesis simulations of an electron transport system (ETS) for the MOCCA detector at CSR have been presented and discussed. The purpose of the ETS is to guide secondary electrons, induced by electrically neutral molecular fragments impinging on the micro-calorimeter detector MOCCA, towards a fast-timing detector. This allows reading out the relative impact times between the fragments and thus enables 3D fragment-imaging for the MOCCA detector. The electrons are supposed to transfer the impact timing difference of fragments onto the fast-timing detector - an MCP. This transfer is successful if firstly the relative timing information of fragments is conserved by the electrons and if secondly the electrons can be assigned to their respective inducing fragments. The goal of this thesis has been to provide a feasibility study of the ETS by addressing these two major questions, as stated in section 1.4.

Accomplished simulations within a simplified model of the ETS as described in section 3 qualitatively approved the working principle of the ETS. This led to simulations of a detailed, realistic model of the ETS as described in section 4. In these simulations the trajectories of electrons emitted at all possible positions within the detection area of MOCCA were calculated. Initial conditions for secondary electrons have been randomized following realistic distributions of kinetic energy and polar angle towards the normal detector surface, as described in section 2.1. Recording the final position and TOF of electrons when they arrived at the MCP gave rise to the following results: The electron TOF values were distributed around 4.96 ns. This distribution showed a FWHM of ≈ 30 ps, which is small compared to the typical difference of $\lesssim 100$ ns in arrival times of fragments at MOCCA. Therefore conservation of the fragment timing information by secondary electrons was demonstrated within this realistic model of the ETS.

In addition to that, for each initial electron position at MOCCA the resulting spatial electron distribution at the MCP, i.e. the distribution of possible final electron positions, was investigated. Each distribution was characterized by its centroid and its size. Their shape was assumed to be elliptic with an orientation of the semi-minor axis along the wires of the acceleration harp. The defined quantity *shift* (displacement between initial position and centroid position) revealed that it does not lead to mixing of spatial electron distributions of different initial positions.

Considering an overlap of the elliptic spatial distributions, the defined quantity *spread* (mean distance between centroid and individual final electron position) quantified the semi-axes of these ellipses for each initial position. Averaging over the whole detection area, the mean spread was used as dimensions of typical spatial electron distributions, resulting in $\overline{s_x} = 1.82$ mm and $\overline{s_y} = 2.53$ mm for the semi-minor and semi-major axis, respectively. From these results it is concluded that for fragment impact distances larger than $2\,\overline{s_x} = 3.64$ mm along the wires and $2\,\overline{s_y} = 5.06$ mm normal to the wires, the secondary electrons, and their timing information, can likely be assigned to their parent fragment impacts. These dimensions, compared to detection area of 44.8 mm $\times$ 44.8 mm, result in a good relative spatial resolution of the ETS, which in turn leads to a good timing assignment capability of the setup.

In addition to the work presented in this thesis, the author has also investigated the possibility of focusing the electrons within the ETS such that a smaller area would be covered in the MCP plane. Due to external geometrical limitations such a possibility would simplify the ETS design. In short, a configuration for such focusing was realized by electrically separating the acceleration harp from the drifttube. While acceleration voltage was kept, a lower potential on the drifttube resulted in the focusing effect. While the quality of the focused projection was comparable to the non-focused case, the relative spatial resolution degraded when compared to the non-focused implementation. A compromise between the MCP size and the resolution quality must still be found.

In the future even more realistic simulation of the ETS could surely be achieved. E.g., the wires of the involved harps could be modeled as non-transparent. Moreover, for construction/mechanical reasons the harps may be replaced by grids, leading to a change in the micro lensing effect. However, it is expected that such modifications would lead only to minor quantitative changes and the qualitative behavior of the ETS would not be affected.

As the next step it is proposed to use the results of the ETS Monte-Carlo simulations as test data for developing and optimizing an algorithm for assigning the MCP-detected electrons to the MOCCA-detected molecular fragments. Here the basic approach will be to first group all detected electrons by their impact times. Each group is expected to represent one impact fragment on the MOCCA. For each such electron group a mean MCP position will be used for mapping to the fragment impact positions on MOCCA and the electron-to-fragment assignment. Special care will be needed in cases of close impact times or impact positions. The algorithm will also get increasingly complicated as the number of impact fragments rises.

Finally it is concluded that the simulations within this thesis successfully demonstrated the capability of the ETS to realize fast-timing-readout for the micro-calorimeter based MOCCA detector. This will enable 3D fragment-imaging capability of this detector and thus extend the range of accessible physical quantities in the CSR measurements. The simulations lead to detailed technical design of the ETS. Physical implementation of MOCCA with ETS will take place in a dedicated test setup in a near future. Afterwards, the detector may finally be put to work in the CSR with the advantage of 3D fragment-imaging.

References

[1] R. Feynman, R. Leighton, and M. Sands. “The Feynman Lectures on Physics”. In: vol. I. Basic Books, 1963. Chap. 1 - Atoms in Motion. URL: `http://www.feynmanlectures.caltech.edu/i_01.html` (visited on 09/02/2017).

[2] R. von Hahn et al. “The cryogenic storage ring CSR”. In: *Review of Scientific Instruments* 87 (2016).

[3] O. Novotný et al. “Cryogenic micro-calorimeters for mass spectrometric identification of neutral molecules and molecular fragments”. In: *Journal of Applied Physics* 118 (2015).

[4] L. Gamer et al. “MOCCA: A 4k-Pixel Molecule Camera for the Position- and Energy-Resolving Detection of Neutral Molecule Fragments at CSR”. In: *Journal of Low Temperature Physics* 184 (2016).

[5] M. De Cesare et al. “A TOF-E detector for ERNA recoil separator”. In: *Journal of the Italian Astronomical Society* 78 (2007).

[6] *Homepage of software product SIMION® by Scientific Instrument Services, Inc. (SIS)*. URL: `simion.com` (visited on 01/31/2018).

[7] D. Hasselkamp et al. “Particle Induced Electron Emission”. In: vol. II. ©Springer-Verlag Berlin Heidelberg, 1992. Chap. Kinetic Electron Emission from Solid Surfaces Under Ion Bombardment.

[8] Raúl A. Baragolia. “Principles and mechanisms of ion induced electron emission”. In: *Nuclear Instruments and Methods in Physics Research* B78 (1993).

[9] D. Hasselkamp, S. Hippler, and A. Scharmann. “Ion-Induced Secondary Electron Spectra From Clean Metal Surfaces”. In: *Nuclear Instruments and Methods in Physics Research* B18 (1987), pp. 561–565.

[10] William H. Press et al. *Numerical Recipes: The Art of Scientific Computing*. 3rd ed. New York: Cambridge University Press, 2007.

[11] *SIMION® Version 8.0/8.1 User Manual*. Nov. 2011.

[12] David J. Griffiths. *Introduction to Electrodynamics*. 4th ed. Pearson, 2013.

[13] *Homepage of software product Solid Edge by Siemens PLM Software*. URL: `https://www.plm.automation.siemens.com/en/products/solid-edge/` (visited on 01/25/2018).

Erklärung

Ich versichere, dass ich diese Arbeit selbstständig verfasst und keine anderen als die angegebenen Quellen und Hilfsmittel benutzt habe.

Heidelberg, den 18. Februar 2018

Sebastian Spaniol